

Diffuse Stellar Light at 100 kpc Scales in M87

Melinda L. Weil

Department of Physics, Oxford University, Astrophysics Building, Keble Road, Oxford
OX1 3RH, United Kingdom

Jonathan Bland-Hawthorn¹ & David F. Malin

Anglo-Australian Observatory, P.O. Box 296, 2121 Epping, NSW, Australia

ABSTRACT

In a new survey of nearby galaxies from stacked photographic images, seemingly regular galaxies of several types show amorphous, often asymmetrical features at very faint levels (28mag arcsec⁻²). In M87, a diffuse fan of stellar material extends along the projected SE (major) axis out to about 100 kpc.

We suggest that accretion of a small spheroidal galaxy into a larger potential is the most likely explanation for the diffuse structure. The orbit is required to pass close to the center of the potential to produce a fan which nearly aligns with the major axis and has a large opening angle, as seen in M87.

Our simulations include a rigid primary potential with characteristics similar to those derived for M87 and a populated secondary potential. We investigate the structure of the dark matter at large galactic radii by representing M87 with different potentials. The morphologies of the debris of intruder spheres and disks of different masses and orbital parameters limit the possible accretion scenarios. The total luminosity of the fan and the kinematics of debris in the center of the primary potential are analyzed and compared with substructure in M87.

The short lifetimes ($t_{fan} \lesssim 5 \times 10^8$ years) of the simulated diffuse fans and lack of observed shells indicates that either we are seeing M87 at a ‘special time’ during its evolution or that infall from small intruder galaxies is common. Our simulations indicate that several accretion events could be hidden in galaxies. For many orbits, intruder material is quickly spread out to very low light levels. Observations of the high specific frequency of globular clusters in M87 provide evidence that the galaxy may experience frequent accretions of this type.

¹Visiting Fellow, Oxford University

1. Introduction

A giant elliptical radio galaxy in the central regions of the nearby Virgo cluster, M87 (NGC 4486) exhibits properties that have stimulated numerous studies at all wavelengths. Nonthermal emission is observed from the radio to the X-ray; the galaxy contains an optical synchrotron jet, a small nuclear disk of ionized gas, and a broad distribution of X-ray emitting gas. The luminous and compact nucleus is thought to surround a supermassive black hole which powers the galaxy’s radio source. Although the Virgo cluster is considered an ideal host for a cooling flow, searches for HI in absorption against the M87 radio source fail to detect any spatially extended distribution (Dwarakanath, van Gorkom, & Owen 1994). The description of M87 as a classical E0 or E1 is based on short exposure optical images; the optical isophotes, however, show marked eccentricity in deeper images.

The extremely uniform sensitivity and large sensitive area of photographic plates make them ideal detectors of faint light sources extended over wide angles. This detectivity can be considerably improved by ‘photographic amplification’ (Malin 1978) and photographic ‘stacking’ or combination of several amplified derivatives (Malin 1988, Bland-Hawthorn, Shopbell, & Malin 1993), extending the detection to about 5 magnitudes below the night sky brightness. With UK Schmidt plates at Siding Spring, this corresponds to a limiting (B) surface brightness of about 28mag arcsec^{-2} . To produce the image of M87 (Figure 1), five deep, IIIa-J (395-530nm passband) UK Schmidt plates were combined.

Immediately apparent is the broad, diffuse and structureless ‘fan’ extending at least 15 arc minutes SE along the major axis of the galaxy. Unfortunately, the image of a bright star (HD 109032, $V=7.9$, F0) lies in this direction and probably adds a little to the extended structure. However, a star of similar visual magnitude (HD 108614, $V=7.95$, K0) lies about 40 arc minutes SW of M87 and has an inner halo hardly visible against the night sky background, so the extended component of M87 evident in Figure 1 is real, though more symmetrical along the major axis than the region contaminated by the star image would suggest.

An extension of M87 was first detected by Arp & Bertola (1969) in commendably deep exposures, which also showed continued isophotal flattening at large radii. These authors suggest that, while the increasing ellipticity of the M87 isophotes is not expected if the galaxy formed by collapse of a primeval cloud in which no angular momentum transport occurs, the elongation could be the result of ejection from the nucleus (Arp & Bertola 1971). The image in the present paper is, however, deeper and emphasizes the asymmetry of M87 at large radii. In it, M87 also appears to have a smaller, more regularly-shaped, caplike extension in the opposite direction to the SE fan.

A concern is whether the extended fan is indeed stellar in origin. Other possibilities include optical line emission or scattered light, both of which would require an associated component of neutral gas. Jura (1980) first suggested that the faint outer parts of spirals could arise as galaxian light scattered by the extended HI disk. His simple model predicted that it would be possible to distinguish between star light and scattered light at a visual magnitude of about 28-29 mag arcsec⁻². At these extremely faint levels, which are barely reachable with stacked photographic plates, it would be impossible to test for linearly polarized light with current technology. However, to explain the diffuse light as dust-scattered radiation from M87 requires high column densities of gas ($\sim 10^{21}$ cm⁻²) with a total HI mass ($\sim 10^{10} M_{\odot}$) which would have easily been detected in previous HI surveys. Therefore, it seems unlikely that the extended emission is associated with gas. Nor has comparable structure been observed in either X-ray or radio maps (*e.g.* Feigelson *et al.* 1987, Bohringer *et al.* 1995).

The present study was undertaken to determine whether production of large-scale diffuse structure, such as seen in this image of M87, and suppression of fine structure is possible in large-mass-ratio accretion events. We explore the idea that the merger of a small intruder is responsible for the newly-discovered diffuse fan in M87. Previous simulations of accretion focus on formation of fine structure similar to that observed in a large fraction of elliptical galaxies (Malin & Carter 1983). However, no shells have been observed in M87. Satellites which are accreted by larger galaxies with mass ratios $M_s/M_p = 0.01 - 0.1$ produce stellar shells and arcs with sharp edges (*e.g.* Dupraz & Combes 1986, Hernquist & Quinn 1988, 1989). If gas is included in a disk intruder, it quickly segregates from the stellar material to produce a clump or ring of gas in the center of the primary (Weil & Hernquist 1993). In these previous models, roughly half of the stellar or gaseous particles are captured by the primary. Little attention has been paid to the balance of the debris.

There is a wealth of evidence for accretion in ellipticals, including observations of multiple cores, shells, large quantities of dust and gas, and kinematic substructure including counter-rotating disks or rings. Kinematic anomalies have been observed in M87; the mean velocity in the central regions is smaller than the inferred systemic velocity (Dressler & Richstone 1990, van der Marel 1994). Rotation curves of high spatial-resolution reveal a kinematically distinct subcomponent within $2'' - 3''$ (150 – 225 pc for $D_{M87} = 15$ Mpc) of the nucleus (Jarvis & Peletier 1991). The blue-shifted annulus has a velocity of 40 km s⁻¹ with respect to the surrounding stars and covers an area of approximately $5''$. This subcomponent may be a dense core or disrupted material from a captured companion which has fallen to the center of M87. In addition, the total number of globular clusters in M87 is ≈ 16000 , giving it a globular cluster specific frequency $S_N = 14$ whereas the typical specific frequency for normal ellipticals in dense regions is $S_N = 4 - 5$ (Harris

1991). West *et al.* (1995) suggest that the excess population of globular clusters in massive ellipticals in clusters may not be bound to the individual galaxy. Instead, the globular clusters occupy the cluster center as a whole, having been tidally stripped from their parent galaxies during interactions or having originated in high-density regions of the cluster core itself. However, if accretion of small spheroids with 5 – 10 globular clusters each is common over the lifetime of the galaxy, the excess population may be bound. Dynamical friction considerations suggest that globular clusters, with many times the mass of a single star, could be stripped from the intruders and bound to the galaxy potential while much of the other stellar material escaped or was dispersed.

In the following section, the methodology for constructing primary and secondary potentials is presented, drawing on observations of M87 and of small elliptical and disk galaxies. § 3 presents the results of varying the initial conditions of the primary and intruder system and compares the structure of several models to M87 properties. In § 4 we discuss the results.

2. Methodology

The initial systems which we evolve comprise two galaxies: a massive elliptical which is intended to resemble M87 and a small intruder sphere or disk. A large number of free parameters are available for exploration and an attempt must be made to constrain the parameter space. Primary galaxy construction requires assumptions about the total mass, the shape of the potential, and relevant length scales. We use recent observations of M87 to determine reasonable estimates for these quantities. The intruding galaxy introduces a further number of free parameters into the simulations: galaxy type, mass, scale length, and the initial orbital position and velocity.

2.1. Properties of M87

At a distance of 15 Mpc, $1'' = 75$ pc and $1' = 4.5$ kpc in M87. Figure 2 shows an image of M87 from the Digital Sky Survey. Visual band surface photometry of the stellar emission shows that eccentricity increases from $\approx 10\%$ around $1'$ to $\approx 40\%$ around $3'$ and remains this flattened beyond $30'$ (Carter & Dixon 1978). Axis ratios measured directly from Figure 2 are $c/a = 1$ at $x = 3.4$ kpc and $c/a = 0.85$ at $x = 12$ kpc, where x is defined along the major axis. From Figure 1, the axis ratio at $x \approx 50$ kpc is $c/a \approx 0.6$.

The velocity dispersion of M87 is known to rise from about 300 km s^{-1} at 750 pc

to 360 km s^{-1} in the center (*e.g.* Dressler & Richstone 1990). Long-slit spectrograph observations out to 13 kpc show that the velocity dispersion declines from $\approx 375 \text{ km s}^{-1}$ in the center to $\approx 325 \text{ km s}^{-1}$ at 2.2 kpc, rises to $\approx 350 \text{ km s}^{-1}$ at about 3.7 kpc, and then declines to $\leq 300 \text{ km s}^{-1}$ (Sembach & Tonry 1996). The zero point of the Sembach & Tonry dispersion is $\approx 6\%$ higher than that of previous published studies; this is most likely due to broadening associated with the large slit. At large distances from the center, there are velocity dispersion anomalies which deviate from a smoothly declining profile. These deviations may be caused by components with velocity dispersions that differ from that of the underlying galaxy. Although Sembach & Tonry do not impute any significance to the deviations, the anomalies might be attributable to accreted material. However, given the accuracy of the observations, an approximately constant velocity dispersion from 7 – 13 kpc cannot be ruled out.

Eccentricity in residual X-ray surface brightness isophotes along a NE–SW axis was discovered by Feigelson *et al.* (1987) after subtracting the axisymmetric component. They note that the gravitational potential, which is dominated by nonluminous mass at large distances from the center, is expected to affect the X-ray gas as well as the stellar component. The ROSAT images of Bohringer *et al.* (1995) show that a few percent of the X-ray luminosity resides in a roughly linear structure extending across $10'$. A comparison with a radio map of M87 shows that this thermal linear feature coincides with radio features in the outer halo and may be due to emission from cooled gas along the radio jets rather than a response to the static gravitational potential. Thus, there is no strong constraint for the shape of M87 at 100 kpc scales.

The enclosed mass at large radii has been calculated using X-ray data and the kinematics of the globular cluster system. Fabricant & Gorenstein (1983) find $1.2 - 1.9 \times 10^{13} M_{\odot}$ within $20'$ (90 kpc), and $3.0 - 6.0 \times 10^{13} M_{\odot}$ within $60'$ (270 kpc). The ratio of mass to luminosity increases from $M/L = 5 - 15$ at $1'$ to $M/L = 50$ at $10'$ and to nearly $M/L = 200$ at $20'$, indicating that X-ray gas only accounts for about 5% of the dark matter in M87. Stewart *et al.* (1984) calculate the mass distribution using a number of models, all of which converge to $M = 3 \times 10^{13} M_{\odot}$ within $50'$. Merrit & Tremblay (1993) use globular cluster velocities to constrain models of the dark matter distribution and find $6_{-1}^{+4} \times 10^{12} M_{\odot}$ within 50 kpc, in agreement with the X-ray data.

Calculation of the core radius of M87 proceeds by assuming that the dark matter core radius is similar to that of the globular cluster distribution. There is fairly good agreement among different researchers, with values $R_c = 4.6 \pm 0.5$ kpc, 5.8 kpc, and 6.6 ± 0.4 kpc (McLaughlin 1995, Merritt & Tremblay 1993, Lauer & Kormendy 1986, respectively). The large core of the globular cluster distribution likely represents the underlying dynamics of

the formation epoch, as it appears unrelated to the luminous mass, and may be expected to reflect the dark matter distribution. However, these results do not rule out a significantly different value for the core radius; for example, Stewart *et al.* (1984) suggest $R_c \approx 25$ kpc from models fit to the X-ray surface brightness distribution and spectroscopic measurements of the Fe lines. For comparison, the half-light radius of the stars in M87 is 7.2 kpc and the core radius is an order of magnitude smaller.

2.2. Properties of the Primary Potential

2.2.1. Logarithmic potential

The axisymmetric logarithmic potential introduced by Binney (1981) represents a galactic halo with a density that falls as r^{-2} at large radii with

$$\Phi(R, z) = -\frac{1}{2}v_0^2 \log \left(R_c^2 + R^2 + \frac{z^2}{q^2} \right) \quad (1)$$

where R_c is the core radius, $v \rightarrow v_0$ at large r , and q is the axial ratio of spheroidal equipotentials. This model was chosen because the axis ratios of the surface density contours decrease with radius as is observed for the luminous material of M87. The logarithmic potential models have a positive definite distribution function for oblate galaxies with q in the range $0.707 \leq q < 1.0$ and for prolate galaxies with $1.0 < q \leq 1.08$; $q = 1.0$ produces a spherical halo (*e.g.* Evans 1993). The cumulative mass distribution $M(r) = 4\pi \int_0^r \rho(r') r'^2 dr'$ is a function of R_c , v_0 , and q through the density

$$\rho(R, z) = \frac{v_0^2}{4\pi G q^2} \frac{(2q^2 + 1) R_c^2 + R^2 + (2 - q^{-2}) z^2}{(R_c^2 + R^2 + z^2 q^{-2})^2}. \quad (2)$$

For models with $q = 1.05, 0.975, 0.900$ and 0.850 and a core radius $R_c = 6.0$ kpc, the requirement that the calculated masses resemble those measured from M87 X-ray data at large radii helps constrain v_0 . Taking the lower limit on the mass of M87 of $M(R = 120 \text{ kpc}) \approx 5 \times 10^{12} M_\odot$ and $M(R = 240 \text{ kpc}) \approx 10^{13} M_\odot$ requires $v_0 \approx 400 \text{ km s}^{-1}$. $M(R = 240 \text{ kpc}) \approx 3 \times 10^{13} M_\odot$ implies $v_0 \approx 650 \text{ km s}^{-1}$.

The projected surface density is calculated from

$$\Sigma(x, y) = \frac{v_0^2 q}{4G} \frac{x^2 + y^2 + R_c \left(1 + \cos^2 i + q^2 \sin^2 i \right)}{\left[(x^2 + R_c^2) \left(\cos^2 i + q^2 \sin^2 i \right) + y^2 \right]^{3/2}} \quad (3)$$

for an inclination angle $i = 90^\circ$. The axis ratios for a $q = 0.850$ logarithmic potential at $x = 3.5, 12,$ and 50 kpc are $c/a = 0.80, 0.70,$ and 0.65 , respectively. For comparison, the axis ratios at the same x for $q = 0.900$ are $c/a = 0.85, 0.80,$ and 0.75 .

2.2.2. Hernquist potential

For comparison, models are also generated from axisymmetric Hernquist potentials (Hernquist 1990). These models provide good fits to the $R^{1/4}$ law light distribution in elliptical galaxies. The local mass density is found from

$$\rho = \frac{M}{2\pi abc} \frac{1}{\mu (1 + \mu)^3} \quad (4)$$

where

$$\mu^2 = \frac{x^2}{a^2} + \frac{y^2}{b^2} + \frac{z^2}{c^2}. \quad (5)$$

The potential for axisymmetric cases is not analytic,

$$\Phi = -\frac{GM}{2} \int_0^\infty \frac{du}{\Delta(u)(1 + m(u))^2} \quad (6)$$

where $\Delta(u) = ((a^2 + u)(b^2 + u)(c^2 + u))^{1/2}$ and

$$m(u) = \frac{x^2}{a^2 + u} + \frac{y^2}{b^2 + u} + \frac{z^2}{c^2 + u}. \quad (7)$$

The enclosed mass is

$$M(\mu) = M_{total} \frac{\mu^2}{(1 + \mu)^2}. \quad (8)$$

We tested models with spherical shapes: $a = b = c = 1$; oblate shapes: $a = b = 1$, $c = 0.6$ and $c = 0.8$; and prolate shapes: $a = 1$, $b = c = 0.6$ and $b = c = 0.8$. The axis ratios are constant and allow a comparison with the effects of the varying axis ratios of the logarithmic potential.

Whereas the logarithmic potential has a large core defined by the value R_c , the Hernquist potential is cuspy. The top frame of Figure 3 shows the density profile for the two potentials with their masses normalized to $M_{total} \approx 3 \times 10^{13} M_\odot$ at large radii. For the logarithmic potential, the thin line represents $R_c = 6$ kpc and the thick line $R_c = 25$ kpc, and the half-mass radius is approximately 120 kpc. For the Hernquist potential, the spherical model and the axisymmetric model with $c/a = 0.8$ have similar density profiles in this representation. The thin and thick lines represent models with $a = 6$ kpc and $a = 25$ kpc, respectively, where the half-mass radius is found from $r_{1/2} = (1 + \sqrt{2})a$ in spherical potentials.

2.2.3. *Plummer and perfect potentials*

For further comparison, models with Plummer and perfect potentials are constructed. Both of these models have finite cores. The density of the spherical Plummer model is

$$\rho = \frac{3M}{4\pi a^3(1 + r^2/a^2)^{5/2}} \quad (9)$$

and that of the perfect model is

$$\rho = \frac{Ma}{\pi^2(a + r)^2}. \quad (10)$$

These models are shown in the bottom frame of Figure 3, where the thin and thick lines represent the different values for a as above. In the same panel, the density profiles of the axisymmetric perfect model with an axis ratio $c/a = 0.8$ and the isochrone model with a linear scale-length of 6 kpc are shown for comparison.

2.3. Properties of the Secondary Potential

In the attempt to account for the broad, diffuse fan in M87 and the apparent lack of sharp-edged fine structure, we focus on encounters that might be expected to suppress strong shell formation. Debris from the disruption of disk companions tends to show sharp-edged features even in the escaping stellar tails (*e.g.* Weil & Hernquist 1993, Figure 2). In addition, little or no H I appears to exist in M87. Observations of gas and dust in ellipticals indicate that they are accreted in mergers. The H I content of ellipticals is usually contained in disks or rings in a nuclear condensation or outside the optical boundaries of the galaxy; these structures are often rotationally supported, with larger specific angular momenta than the stars. Even small disks contain enough neutral gas ($M_{gas} \sim 10^9 M_\odot$) to pollute gas-poor early-type galaxies. Both of these considerations suggest that the galaxy responsible for M87’s diffuse fan was probably a spheroid.

A Plummer model with

$$\Phi = -\frac{GM_s}{(r^2 + a_s^2)^{1/2}} \quad (11)$$

is used to represent small spheroids. 10,000 particles are randomly distributed in a sphere of radius $3 - 5a_s$. Because spheroids are supported by velocity dispersion, the initial velocities are set to approximate virial equilibrium. Masses of $2 \times 10^9 - 2 \times 10^{10} M_\odot$ and scale lengths of 300 – 1200 pc are considered.

In order to test the influence of intruder type, we also simulate an infalling disk. The disk has particles which are distributed according to an exponential surface density profile.

The total mass is 10^{-4} times the primary mass, the potential scale length is 2 kpc, and the density scale length is 1.5 kpc. The disk stars are rotationally supported with velocities initialized to provide centripetal equilibrium in the secondary potential. As the effects of velocity dispersion are ignored, stars follow circular orbits in the small galaxy until it is tidally distorted by the primary.

2.4. Evolution Code

In the evolution of the systems, the primary galaxy is treated as a rigid potential whereas the small galaxy is rigid but populated. The code uses a variant of a restricted 3-body method which solves the two-body problem of the primary and secondary potentials, based on the initial orbital parameters provided for each encounter. For some models, as with the axisymmetric Hernquist potential whose acceleration is not analytic, the code is joined with the self-consistent field method (Hernquist & Ostriker 1992) in which the primary density and potential are expanded in a set of basis functions in order to solve Poisson’s equation. A leapfrog integrator is used to compute the positions and velocities of the center of mass of the galaxy and intruder at equal timesteps. Then, the positions and velocities of particles are updated by interpolating the tabulated phase-space coordinates for the two-body system to calculate the acceleration. The small and primary galaxies are initially separated by a sufficiently large distance that tidal effects are negligible.

The response of the secondary to the disrupting influence of the primary must be considered. In previous simulations of large-mass-ratio accretions, a ‘disruption radius’ is chosen (*e.g.* Hernquist & Quinn 1988, 1989). When the intruder reaches a distance $r_{disrupt}$ from the primary, the potential used to represent the small galaxy vanishes and the particles evolve in the solitary gravitational field of the primary. A concern in these simulations is whether the choice of disruption radius strongly affects the subsequent evolution of the particles. For previous simulations of shell formation Heisler and White (1990) noted that, while the populations of shells depend on the details of disruption of the companion, positions of shells depend only on the potential of the primary. However, for any one orbit, the opening angle of the ‘fan’ is determined by the differences in the tidal force felt by the distribution of intruding particles. The different distances of closest approach to the primary potential center will produce different velocities perpendicular to the original orbit for each particle, and the tidal encounter will also induce different velocities along the original orbit. Thus, the opening angle will depend on the range of the ratio of these two velocities.

A more self-consistent treatment, which takes dynamical friction into account, is

necessary to achieve the correct binding energy distribution. Here, we compare several methods: 1) specifying an instantaneous disruption radius, 2) allowing the secondary potential to survive the encounter with the large galaxy even when the constituent particles of the intruder are torn away, and 3) slowly disrupting the secondary potential by reducing its mass as particles become unbound. For the first method, a two-body integration is used to determine the distance of closest approach which then becomes $r_{disrupt}$.

3. Results

Three main ideas motivated the evolution of these models. First, we determine whether diffuse structure on scales of 100 kpc is produced during the merger of a low mass intruder with a large elliptical galaxy. Following that, we determine whether our models can constrain the shape of M87’s potential; that is, is it oblate or prolate and does the observed variance of the axis ratios extend into the non-luminous matter? Finally, we attempt to use the persistence of the diffuse fan to estimate the time since the most recent accretion event and to place limits on the number of recent accretions. Several initial systems were simulated and evolved in order to test the effects of such characteristics as 1) the shape of the primary potential, 2) the initial orbit, 3) different intruder masses and scale lengths, 4) spheres versus disks, and 5) the disruption radius. These effects are discussed below and specific cases which produce structure resembling that discovered in M87 are presented in detail.

The velocity dispersion of the Virgo cluster is $\sigma = 632 \pm 41 \text{ km s}^{-1}$ (Fadda *et al.* 1996). Thus, we might expect the nearby companions of M87 to have large relative velocities. This would lead to high-velocity, plunging mergers if the orbit of a small galaxy passed close to the center of M87. It is likely that M87 has previously devoured nearby companions which might spiral slowly into its gravity well and that its present source of merger material is small galaxies that have been diverted from their original orbits by its deep potential well. Therefore, in most of the simulations the initial separation distance between the two galaxies is 120 kpc and the intruder has zero initial velocity relative to M87. At the distance of closest approach, the relative velocity is very large, $v \gtrsim 1000 \text{ km s}^{-1}$.

The primary + intruder systems are evolved for at least several times 10^8 years. During the evolution, the small galaxy plunges into the primary potential, passing near to its center, and is disrupted. Generally, nearly all of the stars form a spray of material at 100 kpc scales, whose opening angle is dependent on the initial orbital parameters and the shape of the primary potential. Some of this material eventually escapes the gravitational well of the primary, becoming too diffuse for detection at the present limits on timescales

of the order of a few hundred million years. The balance of the stars form finer structure nearer the center of the galaxy, often forming shells at late times. However, previous to forming shells, on their second passage through the center of the galaxy, the intruding particles often form another diffuse extension, opposite to the fan, which sometimes appears similar to that in M87.

3.1. Varying Initial Conditions

We first examined the effect on the evolution of diffuse structure of discontinuing the secondary potential’s attraction for its test particles. Several identical systems were evolved with an $r_{disrupt}$ defined by the distance of closest approach, with no disruption radii, or with slow disruption as the secondary mass is decreased by the mass of its unbound particles. For some potentials and orbital parameters, there is little effect regardless of which method of disruption is used. When the secondary potential remains intact, particles continue to be accelerated along the orbit of the intruder long after it has been destroyed. Slight enhancements of density along the orbit are noticed at late times; however, models with no disruption and slow disruption produce fans of the same size and shape. Because some models only produced healthy fans when the secondary was turned off at $r_{disrupt}$, only models with the other two methods of disruption are considered.

Tests of different initial positions, whose orbits have different distances of closest approach to the primary center, indicate that only orbits which pass near the center produce diffuse fans which resemble that of M87. However, the slight offset of the fan in M87 from the major axis suggest that the encounter was not strictly radial. The distances of closest approach vary from some 10s of parsecs to roughly 1 kpc for the simulations discussed below; however, there is no correlation between the opening angles of the fan and the distances of closest approach. In all the models, the intruder passes close enough to the center of the primary that the subsequent spread of the particles is not primarily dependent on the differences in closest approach. Other tests with a disk intruder are shown to produce fans which have sharp edges, unlike that in M87. Of the several models we evolved, a selection which encourages comparisons between different initial conditions have their properties summarized in Table 1. In the second and third columns, the primary and secondary masses are listed; the fourth column contains the scale length of the secondary. The fifth and sixth columns contain the initial positions. In the seventh column, a description of the primary is given.

To test the effect of different distributions of mass, primary potentials with large and small cores and with cusps were constructed. For the logarithmic potential, models with

different degrees of flattening, $q = 1.0, 0.90$, and 0.85 , were considered. The mass of these galaxies is $M_p = 1 - 3 \times 10^{13} M_\odot$ at 240 kpc and the core radius is 6 kpc, similar to the values for M87. Intruders with masses $M_s = 10^9 - 10^{10} M_\odot$ and scale lengths $a_s = 0.3 - 1.2$ kpc are released from the position $x_i = 119$ kpc, $y_i = 0$ kpc, and $z_i = -13.7$ kpc, a distance of 120 kpc from the center. There were no important differences in the evolution of models with no disruption and models which were disrupted slowly.

The top panels of Figure 4 show three times during the evolution of Run L1, which has a spherical logarithmic primary with $q = 1.0$ and a secondary with mass $M_s = 1.2 \times 10^{10} M_\odot$ and scale length $a_s = 1200$ pc. The middle three panels show Run L2, the same as Run L1 except with a flattened primary of $q = 0.85$. The length of each panel is 360 kpc and times in simulation units, of which one equals 1.2×10^6 years, are shown at the top of each. The ellipses show the shape of the primary surface density at $x = 50$ and 120 kpc in the $x - z$ plane; as do M87's, the isophotes flatten with increasing distance from the center. The accelerations on the intruder as it passes near the center of the logarithmic potential are not sufficient to cause the particles to spray into a fan as in M87; instead a very thin extension is produced. Similar results are found for the other tests of the logarithmic potential, including a prolate model with $q = 1.05$; no wide fans were produced. However, the debris does not evince any fine structure. These high-mass ratio accretion events do not form shells, which is encouraging for our hypothesis that such events can account for diffuse structure in galaxies that have no shells.

In order to test the effect of the large core of the logarithmic potential on the subsequent distribution of debris from the intruder, a similar model with $q = 0.85$ but $R_c = 2.0$ kpc was evolved. The bottom panels of Figure 4 show three times during the evolution of this model. A fan with a wider opening angle is produced; however, it is not comparable in size to that of M87.

In Figure 5, the results for three spherical models with greater central concentrations of mass are shown. The intruder particles are shown after they have passed through the center of the potential and have spread significantly. The model in the top row, Run H1, has a Hernquist primary potential. The model in the middle row, Run P1, has a Plummer primary, that in the bottom row, Run P2, a perfect primary. Each has $M_p \approx 3 \times 10^{13} M_\odot$ at 240 kpc, a scale length of 6 kpc, and an intruder like those described for the models in Figure 4. The Plummer and perfect models with finite cores produce diffuse fans, but ones with smaller opening angles than that produced by the cuspy Hernquist model. Nearly all of the intruder debris forms a large, diffuse fan with an opening angle similar to that of M87 and which travels along a narrow cone at a small angle from the long axis of the galaxy, as is seen in M87. The finer structure, such as shells, that is not observed in M87 is

suppressed.

The effect of flattening and the shape of the primary were further explored for systems whose primary galaxies were constructed from a Hernquist potential. Figure 6 shows the evolution of Run H2 in the $x - z$ plane for a primary and intruder system similar to Run H1 but with an oblate primary with $c/a = 0.8$. The length of each panel is again 360 kpc and times in simulation units are shown at the top of each panel. The ellipses show the shape of the primary surface density at $x = 50$ and 120 kpc. The top row shows the initial position in the $x - z$, $x - y$, and $y - z$ projections. Subsequent panels show the evolution in the $x - z$ plane. The intruder is destroyed by the tidal forces acting on it. The top panels of Figure 7 shows three times for a model, Run H3, exactly similar to Run H2 but with $c/a = 0.6$, and the bottom panels are for Run H4, a prolate primary with $c/a = 0.8$. It is apparent that the flatter primary restricts the opening angle of the diffuse fan; the velocities perpendicular to the orbit are somewhat inhibited at large distances away from the center of the galaxy. Although the accelerations of axisymmetric Hernquist potentials are not analytic, equations 6 and 7 imply that $\frac{da_x}{da_z}$ is proportional to factors of x/z and c/a . Comparing Run H3 with Runs H1 and H2 indicates that, after the intruder passes through the center of the galaxy, the compression of the potential along the minor axis ensures reduction of the spread of accelerations in the z -direction. That a fan comparable to that of Run H2 is produced by the prolate primary of Run H4 suggests that it will be difficult to place strong limits on the shape of M87.

The mass of the intruder also has an effect on the shape of the disrupted material. In previous models, the small galaxy had mass $M_s = 1.2 \times 10^{10} M_\odot$ and scale length $a_s = 1.2$ kpc. The top panels of Figure 8 show results for Run H5 in which a smaller intruder has $M_s = 1.2 \times 10^9 M_\odot$ and scale length $a_s = 300$ pc. The middle panels show results for Run H6 in which the intruder has $M_s = 6.0 \times 10^9 M_\odot$ and scale length $a_s = 600$ pc. The bottom panels of Figure 8 show the fan produced by Run H7, which has a much more massive intruder with $M_s = 6.0 \times 10^{10} M_\odot$ and scale length $a_s = 2.0$ kpc. A comparison with Run H2, in Figure 6, shows that one effect of increasing intruder mass is to increase the opening angle of the diffuse fan. By time 105, 1.3×10^8 years after the initial time, one half of the mass is no longer bound to the secondary galaxy in Runs H5, H6, and H7. At the distance of closest approach, at approximately time 106, the intruder mass has been reduced by a factor of ten. Figure 9 is a velocity histogram for the particles in Runs H5, H2, and H7, in which the top frames are for times when most of the mass is still bound to the intruder and the bottom frames are for subsequent times, when the most of the mass is freely circulating in the potential of the primary. The x -velocity histograms are shaded with horizontal lines; the z -velocity ones are shaded with lines at an angle. It is apparent, in the top frames, that v_z is uniformly small, as expected. In the bottom frames from left to right, after the slow

disruption of the intruder, the spread in v_z increases as secondary galaxy mass increases.

Figure 10 shows the evolution of Run H8 in which the scale length of the primary galaxy is $a_p = 25$ kpc. When the half-mass radius of the galaxy representing M87 is about 60 kpc, the mass distribution is markedly different, as shown in Figure 3; however, a fan, though not one as wide as that of Run H2, is formed. In Figure 11, an intruder with $M_s = 10^{10} M_\odot$ and $a_s = 1.2$ kpc is used, but the mass of the primary is $M_p = 5 \times 10^{12} M_\odot$ at large radii. The top three panels are for a logarithmic primary, the middle ones are for an oblate Hernquist model with $c/a = 0.8$, and the bottom ones are for the same Hernquist model but with the secondary initially positioned 60 kpc from the center of the primary, rather than the fiducial 120 kpc; Runs L3, H9, and H10, respectively. The sizes of the diffuse fans show that reducing the mass of the primary allows production of fans with larger opening angles. In Run H10, the reduced velocity at closest approach restricts the x-extent and z-extent of the fan.

3.2. Evolution at Late Times

In Figure 6, at time 280, the beginning of shell formation is apparent for Run H2 as the tidally ruptured particles oscillate back and forth through the primary. The amount of mass in the diffuse fan decreases with time: while 60% of the intruder particles are in the fan at time 240, only about 30% are at time 280. By time 220, an enhanced diffuse extension is produced opposite to the fan, very similar to the one seen in the image of M87.

Figure 12 shows Runs H1 (top), H2 (middle), and H5 (bottom) at late times in their evolution. In Run H2, by time 340 the fan only contains 20% of the intruder mass and weak, but distinguishable, shell formation is visible. For Run H1, nearly 77% of the intruder mass constitutes the fan at time 260; by time 340, only 32% remains in the fan. While none of these models show very sharp-edged shells, the projected density is enhanced at the turning points of the orbits, where particle velocities are at a minimum. As shown in previous simulations of shell formation, the shells appear to propagate outwards as less tightly-bound particles reach their turning points. No shells have been observed in M87; this fact and information derived from the existence or lack of other substructure may contribute to estimates of the age of the proposed accretion event in M87.

In no case, in all the models, does a strong fan appear for more than a few hundred million years. In the next section, the models which produce fans comparable to that of M87 are more severely constrained; we determine which fans would be visible with the techniques available to us and which produce approximately the amount of light estimated

for the M87 diffuse fan.

3.3. Spatial and Kinematic Structure

The total luminosity in the M87 fan is estimated using the Johnson B band with a zero point of $6.61 \times 10^{-9} \text{ erg cm}^{-2} \text{ s}^{-1} \text{ \AA}^{-1}$ and a band width of 980 \AA . If the distribution of luminosity at $28 \text{ mag arcsec}^{-2}$ is approximately uniform in an area of 300 arcmin^2 , we find $L_{\text{tot}} \approx 3 \times 10^8 L_{\odot}$. This value will be a lower limit if the fan extends further at fainter magnitudes or if there is more diffuse light in the inner regions.

The surface brightness in M_{\odot}/pc^2 of a simulated fan is calculated along a slit with length $l = 300 \text{ kpc}$ laid along the x axis. Particles are distributed onto a Cartesian grid with cell size $\Delta l = 3.75 \text{ kpc}$ in the $x - z$ projection. To calculate the surface brightness in mag arcsec^{-2} in the Johnson B band, a mass-to-light ratio must be assumed in order to transform $\Sigma(M_{\odot}/pc^2)$ to $\Sigma(L_{\odot}/pc^2)$. Then $\mu_B = 24.3 - 2.5 \log(\Sigma)$. In Figure 13, the results for Runs H1, H2, H6, and H9 are shown at two different times. The length of the ordinate axis is 10 magnitudes as shown in the top left frame. The four horizontal lines show $\mu_B = 28 \text{ mag arcsec}^{-2}$ for $M/L = 1, 2, 5,$ and 10 in ascending order as marked on the top right frame. The limiting value for μ_B from the M87 observation is $28 \text{ mag arcsec}^{-2}$ at approximately 110 kpc along the $-x$ axis.

Models with higher-mass intruders than these will not satisfy the observational constraints on the fan’s surface brightness; too much material will be distributed along the $-x$ axis to account for the cut-off at $28 \text{ mag arcsec}^{-2}$ at 100 kpc scales unless the mass-to-light ratio is much larger than $M/L = 10$. This is true, for instance, of Run H7. On the other hand, models like Run H5, with lower-mass intruders, do not create a fan similar to that of M87. The material is not dispersed enough to match the observed distribution of diffuse material.

The last time (dotted line) shown for Run H1 is allowed with $M/L = 10$ because the surface brightness decreases below $28 \text{ mag arcsec}^{-2}$ near 100 kpc , as are the times shown for Run H2. Earlier times, with more mass in the fan, are not acceptable with unless the mass-to-light ratio is larger. Both times shown for Run H6 are acceptable for $M/L = 10$ and 5 . And both times shown for Run H9 are acceptable for $M/L = 10$ and, possibly, 5 . None of these models fit the observational constraints best with a mass-to-light ratio of unity; all must be considered to contain some amount of dark matter. The surface brightness of most model fans has fallen below the observed limit in the Johnson B band by $\approx 7 \times 10^8$ years. Diffuse fans will appear to be transient phenomena at this limit, persisting for only a few

times 10^8 years. Most of the debris will continue to stream into the central regions of the primary galaxy. Some unbound material, however, will disperse into the region surrounding the primary galaxy.

The total luminosity in model fans is determined by calculating the total mass over the area covered by the observed fan. The mass-to-light ratio which is allowed by the observed limiting value of μ_B is applied to transform M_\odot to L_\odot . For Run H1 at time 260, the total luminosity in an area of the fan similar to that of M87 is approximately $L_{tot} = 4 \times 10^8 L_\odot$ with $M/L = 10$. For Run H2 at time 260, it is $L_{tot} = 2 \times 10^8 L_\odot$ with $M/L = 10$. With $M/L = 10$, for Run H6 at time 260, $L_{tot} = 2.1 \times 10^8 L_\odot$ and, at time 280, $L_{tot} = 1.3 \times 10^8 L_\odot$. With $M/L = 10$, for Run H9 at time 210, $L_{tot} = 2.6 \times 10^8 L_\odot$ and, at time 230, $L_{tot} = 1.8 \times 10^8 L_\odot$. The luminosity is twice these amounts if $M/L = 5$. Given the uncertainty in the calculation of total luminosity for the M87 fan, all of these values are acceptable in comparison, although they imply that the mass-to-light ratio of the intruder galaxy is likely close to or larger than $M/L = 5$.

Kinematic anomalies suggest that subcomponents of accreted material may exist in M87. We calculated projected velocity fields for intruder material along slits with length $l = 60$ kpc laid parallel to the indicated axis for Run H6 at time 260 and Run H9 at time 210. The frames of Figure 14 show mean velocity v_r (left) and velocity dispersion σ (right) for intruder debris projected onto an intrinsic plane. The observable line of sight velocities are in the $x - z$ projection (the vantage point from which the fans are similar to that of M87).

The Run H6 and Run H9 v_r results in the $x - z$ projection exhibit deviations from zero, on the order of $50 - 150 \text{ km s}^{-1}$. Interestingly, this is similar to the velocity difference of the kinematically distinct subcomponent seen in M87 by Jarvis & Peletier (1991), but, if observable, the extent of the disturbance is several times larger in the models than is the blue-shifted annulus they see. The debris which resides in the center of the models also has a very large line-of-sight velocity dispersion along the x-slit. The projected dispersions are more than twice as large as those observed in the center of M87. There is little deviation from a smoothly declining profile, and no departures from the profile that could account for those observed using a long-slit spectrograph by Sembach & Tonry (1996). Although it would be serendipitous to exactly reproduce the M87 velocity profiles and although particle number and cell width limit the resolution, these results do demonstrate that mergers which produce diffuse fans may also produce small kinematic disturbances. However, the very large velocity dispersion of the intruder debris will make its influence on the kinematics of the integrated light difficult to detect. Broad shallow wings are easy to miss.

4. Discussion

The discovery of a diffuse fan in M87 motivated this study of the formation of stellar debris at 100 kpc scales through large-mass-ratio accretion. The production of diffuse fans is not constrained by the shape of the primary potential, except in the sense that a very large core prevents their formation. The large core in the logarithmic model prevents the dense central mass concentrations necessary to produce the accelerations that lead to large, diffuse fans of intruder debris. On the other hand, the cuspy Hernquist potential and the higher-density cores of the Plummer and perfect potentials easily form fans with large opening angles. Fans formed during accretion into highly-flattened models are too narrow to resemble the diffuse material in M87; the thin debris is interesting in the context of other of the Deep UK Schmidt Survey galaxies. However, our results do not disallow oblate, prolate, or spherical potentials for M87.

The debris in a spherical Hernquist potential has opening angles large enough to easily account for the distribution of material in the observed M87 fan. Figure 15 shows a composite of M87 and Run H1. Plummer and primary potentials produce comparable but narrower distributions. Although there is no evidence to suggest that the mass density axis ratios in M87 are flattened, as are the photometric axis ratios, the more flattened Hernquist $c/a = 0.8$ models produce debris that resembles the M87 diffuse fan. This is consistent with studies of polar rings around elliptical and S0 galaxies such as NGC 4650A, where polar ring kinematics indicate that the halo has flattened isodensity surfaces with axis ratio $0.3 \leq c/a \leq 0.4$ (Sackett *et al.* 1994). In addition, simulations of merging pairs or groups of spiral galaxies – each with a disk, sometimes a bulge, and a spherical dark-matter halo – produce elliptical-like remnants with flattened halos with $c/a \approx 0.8$ for the pair merger remnants and $c/a \approx 0.8 - 0.9$ for multiple merger remnants (Hernquist 1992, 1993, Weil & Hernquist 1996).

The appearance of the M87 diffuse material does limit the orbital parameters of the merging galaxy; large impact parameter orbits are ruled out. In plunging orbits close to the major axis, the intruder passes near the center of the primary and is disrupted, its debris being spread out along the major axis. If M87 is nearly stationary in the Virgo cluster core, high-velocity accretion events like these could be common. M87 would cannibalize galaxies on radial orbits with respect to the center of the cluster potential. In order to utilize more than morphological information, the characteristics of the intruder debris in likely models are compared to the limiting magnitude of the fan material and observations of kinematic substructure in M87. Large projected velocity dispersions are seen in the $x - z$ plane. Although our resolution does not reach to the 100 pc range as do subarcsec resolution spectra (Jarvis & Peletier 1991, van der Marel 1994), mean velocity can vary

by $50 - 150 \text{ km s}^{-1}$ in the $x - z$ slits near the center. While much of the starlight in the M87 fan is too faint to be accessible to kinematic analysis, embedded planetary nebulae are highly effective tracers (*e.g.*, Hui *et al.* 1995). Planetary nebulae kinematics may allow confirmation of our model out to large radial scales. If these small accretions are common, however, there is no reason to expect that the merger which produced the fan is also responsible for the central v_r variations.

As the disrupted intruder evolves, debris disperses into the region surrounding the primary galaxy. At late times some of the intruder mass remains in low surface brightness ($\mu_B \lesssim 32 \text{ mag arcsec}^{-2}$) features several hundred kpc from the center of the galaxy. This material cannot easily account for a large amount of either halo or intracluster medium mass. As an upper limit, if similar accretions releasing a few $\times 10^9 M_\odot$ occur every 10^8 years, only a few $\times 10^{11} M_\odot$ can be added to the halo or ICM. In addition, because most of the intruder mass remains bound to the primary galaxy, it is unlikely that these encounters can account for the diffuse stellar light seen in clusters (*e.g.* Vilchez-Gomez *et al.* 1994) except in regions within 100 kpc of a large galaxy. While this does not preclude more violent encounters in which most of the intruder is dispersed widely, the diffuse matter can provide only a small fraction of the unseen mass or intracluster light. In the same way, each intruder would be required to contribute a hundred globular clusters to M87 at the rate of one encounter every 10^8 years to account for the observed excess. Because encounters of the types we model here do not leave behind compact remnants, we could not expect to find multiple nuclei in the core of the primary. Several accretion events, in which the intruder material has been dispersed below the threshold of present detection limits, could be hidden in galaxies.

M87 is not unique among massive elliptical galaxies in having a dispersed fan of faint material along its major axis. The Deep UK Schmidt Survey of Nearby Galaxies has uncovered faint stellar structure in NGC 4168 (also in Virgo), NGC 1316 (Fornax A), NGC 2855 and NGC 5266. Several of these ellipticals reveal other evidence for accretion, including dust lanes, extended HI emission, and shells. The spiral galaxies M104 and NGC 4643 are also embedded in a faint halo with diffuse structure. These observations suggest that the dispersal of low-mass intruders over a large area is common (Malin, Weil, & Bland-Hawthorn 1997). This phenomenon has not been recognized previously due to the very low surface brightness of the resulting distribution of material. The debris produced in systems resembling M87 generate kinematic substructure, in addition to low surface brightness, diffuse fans. We expect that future deep studies will continue to reveal diffuse distributions of intruder debris and deviations to kinematic profiles on extended scales. Although spectroscopy below $B = 24 \text{ mag arcsec}^{-2}$ is difficult, one method of uncovering the substructure is to model the underlying smooth elliptical out to the limits of the data and

examine the residuals. Many studies have shown that numerous ellipticals have anomalies in their rotation curves (Jedrzejewski & Schechter 1989, Franx, Illingworth, & de Zeeuw 1991, Fried & Illingworth 1994). Minor axis rotation has been used as a test for triaxiality (Binney 1985). Anomalous changes in major axis rotation curves has been attributed to the capture of a small, compact companion (Jedrzejewski & Schechter 1988). Our observations and simulation results suggest that kinematic disturbance in many ellipticals may be contamination by accreted debris, making probes for higher order structure difficult.

MLW acknowledges funding by a PPARC postdoctoral fellowship. JBH is indebted to Oxford University for a Visiting Fellowship during the summer of 1996. We thank an anonymous referee for pointing out an important early reference which had been missed previously and Tad Pryor for insightful and helpful comments which greatly improved the manuscript.

REFERENCES

- Arp, H. & Bertola, F. 1969, *Ap. Letters*, 4, 23
- Arp, H. & Bertola, F. 1971, *ApJ*, 163, 195
- Binney, J. 1981, *MNRAS*, 196, 455
- Binney, J. 1985, *MNRAS*, 212, 767
- Binney, J. & Tremaine, S. 1987, *Galactic Dynamics* (Princeton: Princeton University press), 45
- Bland-Hawthorn, J., Shopbell, P.L. & Malin, D.F. 1993, *AJ*, 106, 2154
- Böhringer, H., Nulsen, P.E.J., Braun, R. & Fabian, A.C. 1995, *MNRAS*, 274, L67
- Carter, D. & Dixon, K.L. 1978, *AJ*, 83, 578
- Dressler, A. & Richstone, D.O. 1990, *ApJ*, 348, 120
- Dupraz, C. & Combes, F. 1986, *A&A*, 166, 53
- Dwarakanath, K.S., van Gorkom, J.H. & Owen, F.N. 1994, *ApJ*, 432, 469
- Evans, N.W. 1993, *MNRAS*, 260, 191
- Fadda, D., Girardi, M., Giuricin, G., Mardirossian, F. & Mezzetti, M. 1996, *ApJ*, 473, 670
- Feigelson, E.D., Wood, P.A.D., Schreier, E.J., Harris, D.E. & Reid, M.J. 1987, *ApJ*, 312, 101
- Franx, M., Illingworth, G.D. & de Zeeuw 1991, *ApJ*, 383, 112
- Fried, J.W. & Illingworth, G.D. 1994, *AJ*, 107, 992
- Harris, W.E. 1991, *ARA&A*, 29, 543
- Heisler, J. & White, S.D.M. 1990, *MNRAS*, 243, 199
- Hernquist, L. 1990, *ApJ*, 356, 359
- Hernquist, L. 1992, *ApJ*, 400, 460
- Hernquist, L. 1993, *ApJ*, 409, 548
- Hernquist, L. & Ostriker, J.P. 1992, *ApJ*, 386, 375
- Hernquist, L. & Quinn, P.J. 1988, *ApJ*, 331, 682
- Hernquist, L. & Quinn, P.J. 1989, *ApJ*, 342, 1
- Hui, X., Freeman, K.C., Ford, H.C. & Dopita, M.A. 1995, *ApJ*, 449, 592
- Jarvis, B.J. & Peletier, R.F. 1991, *A&A*, 247, 315

- Jedrzejewski, R. & Schechter, P.L. 1988, ApJ, 330, L87
- Jedrzejewski, R. & Schechter, P.L. 1989, AJ, 98, 147
- Jura, M. 1980, ApJ, 241, 965
- Lauer, T.R. & Kormendy, J. 1986 ApJ, 303, L1
- Malin, D. F. 1978, Nature, 276, 591
- Malin, D. F. 1988, in Astrophotography, ed. S. Marx (Heidelberg: Springer-Verlag), 125
- Malin, D.F. & Carter, D. 1983, ApJ, 274, 534
- Malin, D.F., Weil, M.L. & Bland-Hawthorn, J. 1997, AJ, in preparation
- McLaughlin, D.E. 1995, AJ, 109, 2034
- Merritt, D. & Tremblay, B. 1993, AJ, 106, 2229
- Sackett, P.D., Rix, H.-W., Jarvis, B.J. & Freeman, K.C. 1994, ApJ, 436, 629
- Sembach, K.R. & Tonry, J.L. 1996, AJ, 112, 797
- Stewart, G.C., Canizares, C.R., Fabian, A.C. & Nulsen, P.E.J. 1984, ApJ, 278, 536
- van der Marel, R.P. 1994, MNRAS, 270, 271
- Vilchez-Gomez, R., Pello, R. & Sanahuja, B. 1994, A&A, 283, 37
- Weil, M.L. & Hernquist, L. 1993, ApJ, 405, 152
- Weil, M.L. & Hernquist, L. 1996, ApJ, 460, 101
- West, M.J., Côté, P., Jones, C., Forman, W. & Marzke, R.O. 1995, ApJ, 453, L77

Fig. 1.— Image of M87 from photographic stacking of five deep, IIIa-J (395-530nm passband) UK Schmidt plates. The limiting (B) surface brightness is 28mag arcsec^{-2} .

Fig. 2.— Digital Sky Survey image of M87, with length $7'$ and scaling mode set to wrapped linear.

Fig. 3.— Density profiles for several potentials along $x = y = z$. Thin and thick lines are for a core or scale-length of 6 kpc and 25 kpc, respectively.

Fig. 4.— Three times during the evolution of three logarithmic models with masses $M_p = 1 - 3 \times 10^{13} M_\odot$. Top panels show a spherical primary with core radius $R_c = 6.0$ kpc, Run L1; middle panels show a flattened primary with $q = 0.85$ and $R_c = 6.0$ kpc, Run L2; bottom panels show a flattened primary with $q = 0.85$ and $R_c = 2.0$ kpc. The intruders are Plummer models which initially have mass $M_s = 1.2 \times 10^{10} M_\odot$, scale length $a_s = 1200$ pc, and initial positions $x_i = 119$ kpc, $z_i = -13.7$ kpc. The length of each panel is 360 kpc and times in simulation units, one of which equals 1.2×10^6 years, are shown at the top of each.

Fig. 5.— Snapshots of intruder debris for three spherical primaries: Hernquist (top, Run H1), Plummer (middle, Run P1), and perfect (bottom, Run P2). Each has $M_p = 3 \times 10^{13} M_\odot$, $a_p = 6$ kpc, and a Plummer model intruder with $M_s = 1.2 \times 10^{10} M_\odot$, scale length $a_s = 1.2$ kpc, and initial positions $x_i = 119$ kpc, $z_i = -13.7$ kpc.

Fig. 6.— Time evolution for Run H2, an oblate Hernquist potential with $c/a = 0.8$ and the fiducial intruder of Figure 5. The length of each panel is 360 kpc and times in simulation units are shown at the top of each panel. The ellipses show the shape of the primary surface density at $x = 50$ and 120 kpc. The top row shows initial position in the $x - z$, $x - y$, and $y - z$ projections. Subsequent panels show the evolution in the $x - z$ plane.

Fig. 7.— Snapshots of intruder debris for an oblate Hernquist primary with $c/a = 0.6$ (Run H3) and a prolate Hernquist primary with $c/a = 0.8$ (Run H4).

Fig. 8.— Snapshots of intruder debris for three oblate Hernquist primaries with $c/a = 0.8$. In the top panels, the intruder has $M_s = 1.2 \times 10^9 M_\odot$ and $a_s = 300$ pc (Run H5). In the middle panels, the intruder has $M_s = 6.0 \times 10^9 M_\odot$ and $a_s = 600$ pc (Run H6). In the bottom panels, the intruder has $M_s = 6.0 \times 10^{10} M_\odot$ and $a_s = 2.0$ kpc (Run H7).

Fig. 9.— Velocity histogram for Runs H5, H2, and H7, respectively. The top frames are for times at which the particles are bound to the secondary potential; the bottom frames are for subsequent times, when the most of the mass has just become unbound.

Fig. 10.— Time evolution for Run H8, an oblate Hernquist potential with $c/a = 0.8$ but with $a_p = 25$ kpc.

Fig. 11.— Snapshots of intruder debris for primaries with $M_p = 5 \times 10^{12} M_\odot$ and the fiducial intruder. Top panels are for Run L3 with a logarithmic primary. Middle panels are for Run H9, with an oblate Hernquist primary with $c/a = 0.8$. Bottom panels are for Run H10, similar to Run H9 except that $x_i = 59.4$ kpc and $z_i = -8.5$.

Fig. 12.— Evolution of Runs H1 (top), H2 (middle), and H5 (bottom) at lates times.

Fig. 13.— Projected surface brightness profile in Johnson B-band magnitudes for a slit with length $l = 300$ kpc laid along the x axis. The two different times for Runs H1, H2, H6, and H9 are shown chronologically with a dashed and dotted line in each frame. The ordinate axis is 10 magnitudes in length and the effect of varying M/L is represented by the four horizontal lines which show $\mu_B = 28 \text{ mag arcsec}^{-2}$ for $M/L = 1, 2, 5,$ and 10 as detailed in the second frame.

Fig. 14.— Projected velocity fields for Run H6 at times 260 and Run H9 at time 130. Slits of length $l = 60$ kpc are laid parallel to the indicated axis. Frames show mean velocity v_r (left) and velocity dispersion σ (right) for projections onto the $x - z$ planes.

Fig. 15.— M87 overlaid by $x - z$ projection of Run H1 at time 260. Ellipses show the shape of the M87 model surface density at 50 and 120 kpc.

Table 1: Subset of Systems

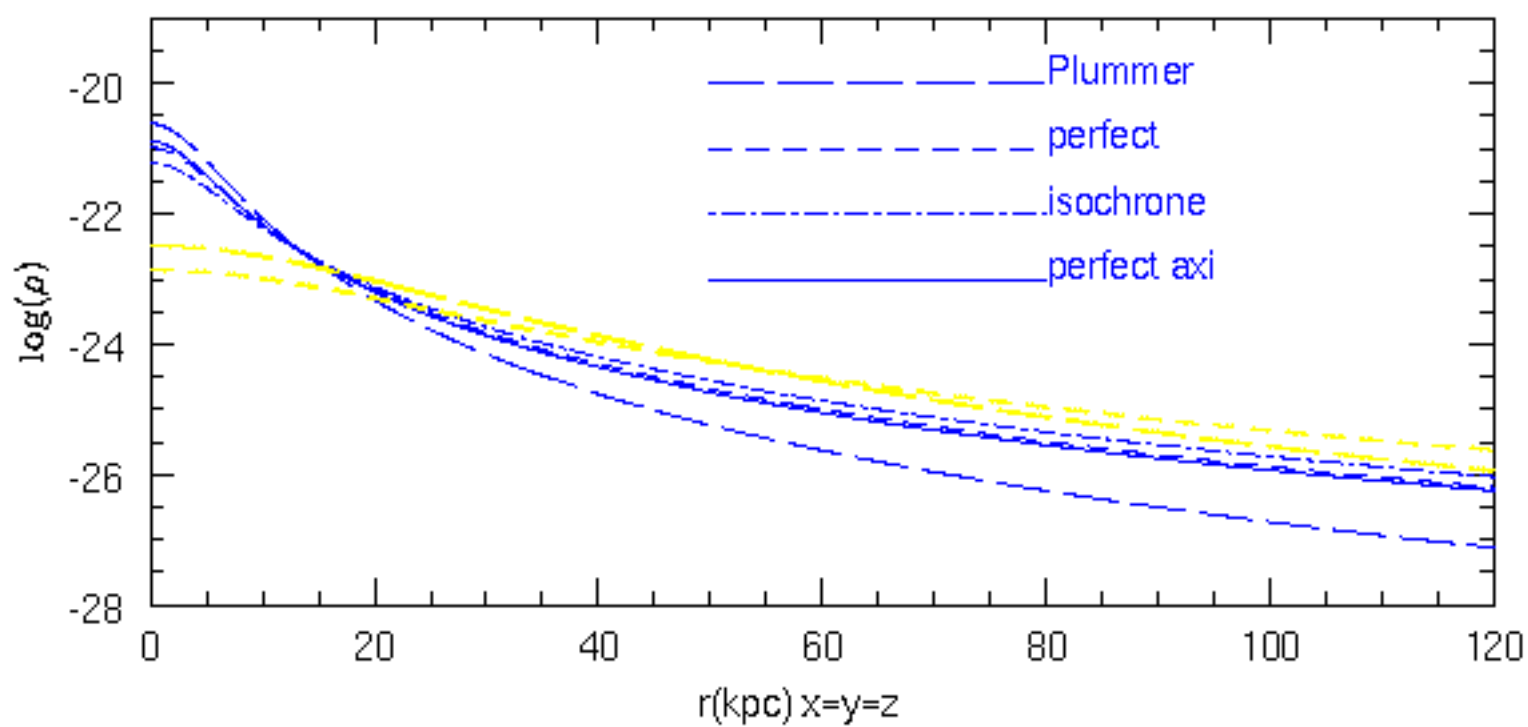
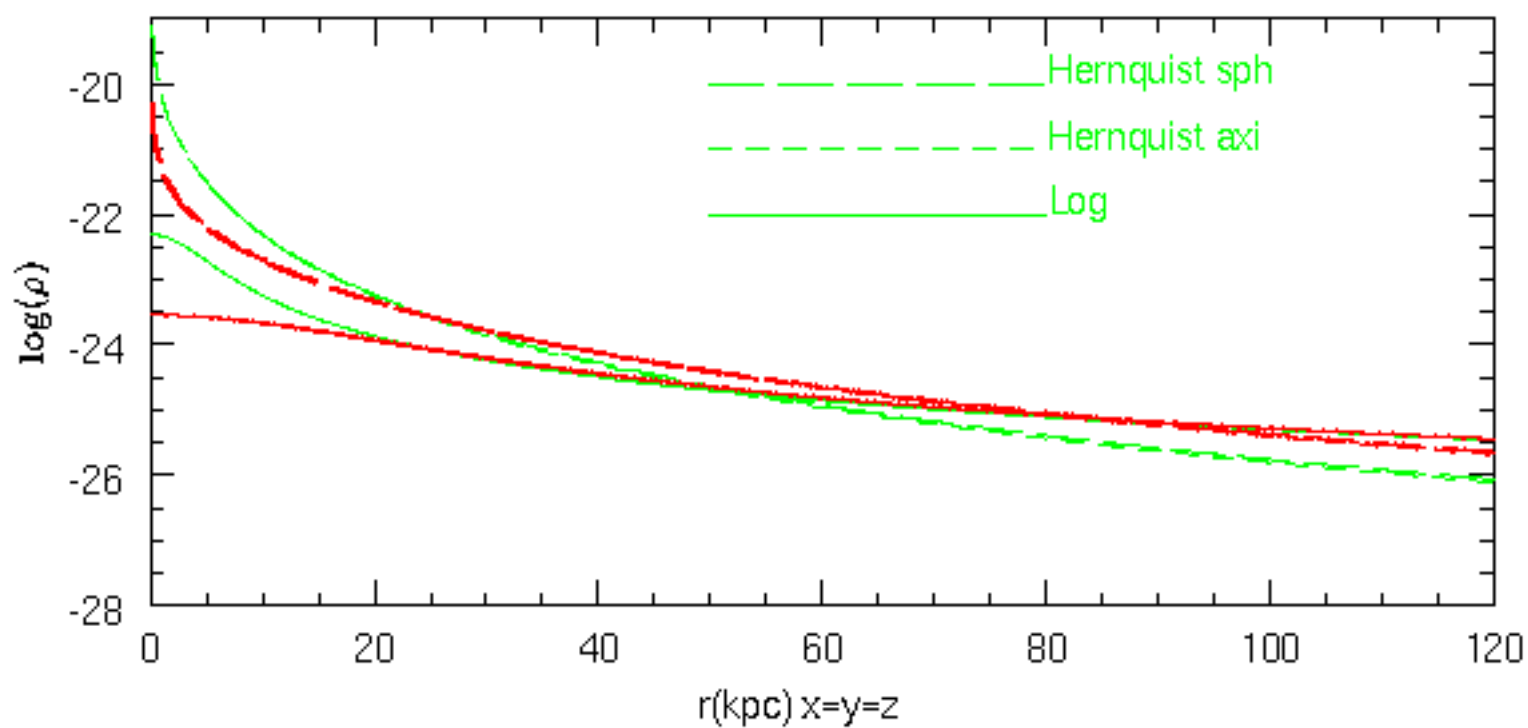
Run	$M_p(M_\odot)$	$M_s(M_\odot)$	a_s (kpc)	x_i (kpc)	z_i (kpc)	Primary
L1	2.4×10^{13}	1.2×10^{10}	1.2	119	-13.7	Logarithmic q=1.0
L2	3×10^{13}	1.2×10^{10}	1.2	119	-13.7	Logarithmic q=0.85
L3	10^{13}	1.2×10^{10}	1.2	119	-13.7	Logarithmic q=0.85
H1	3×10^{13}	1.2×10^{10}	1.2	119	-13.7	Hernquist spherical
H2	3×10^{13}	1.2×10^{10}	1.2	119	-13.7	Hernquist c/a=0.8
H3	3×10^{13}	1.2×10^{10}	1.2	119	-13.7	Hernquist c/a=0.6
H4	3×10^{13}	1.2×10^{10}	1.2	13.7	119	Hernquist prolate
H5	3×10^{13}	1.2×10^9	0.3	119	-13.7	Hernquist c/a=0.8
H6	3×10^{13}	6.0×10^9	0.6	119	-13.7	Hernquist c/a=0.8
H7	3×10^{13}	6.0×10^{10}	2.0	119	-13.7	Hernquist c/a=0.8
H8	3×10^{13}	1.2×10^{10}	1.2	119.5	-11.0	Run H2 with $a_p = 25$
H9	5×10^{12}	10^{10}	1.2	119	-13.7	Hernquist c/a=0.8
H10	5×10^{12}	10^{10}	1.2	59.4	-8.5	Hernquist c/a=0.8
P1	3×10^{13}	1.2×10^{10}	1.2	119	-13.7	Plummer spherical
P2	3×10^{13}	1.2×10^{10}	1.2	119	-13.7	perfect spherical

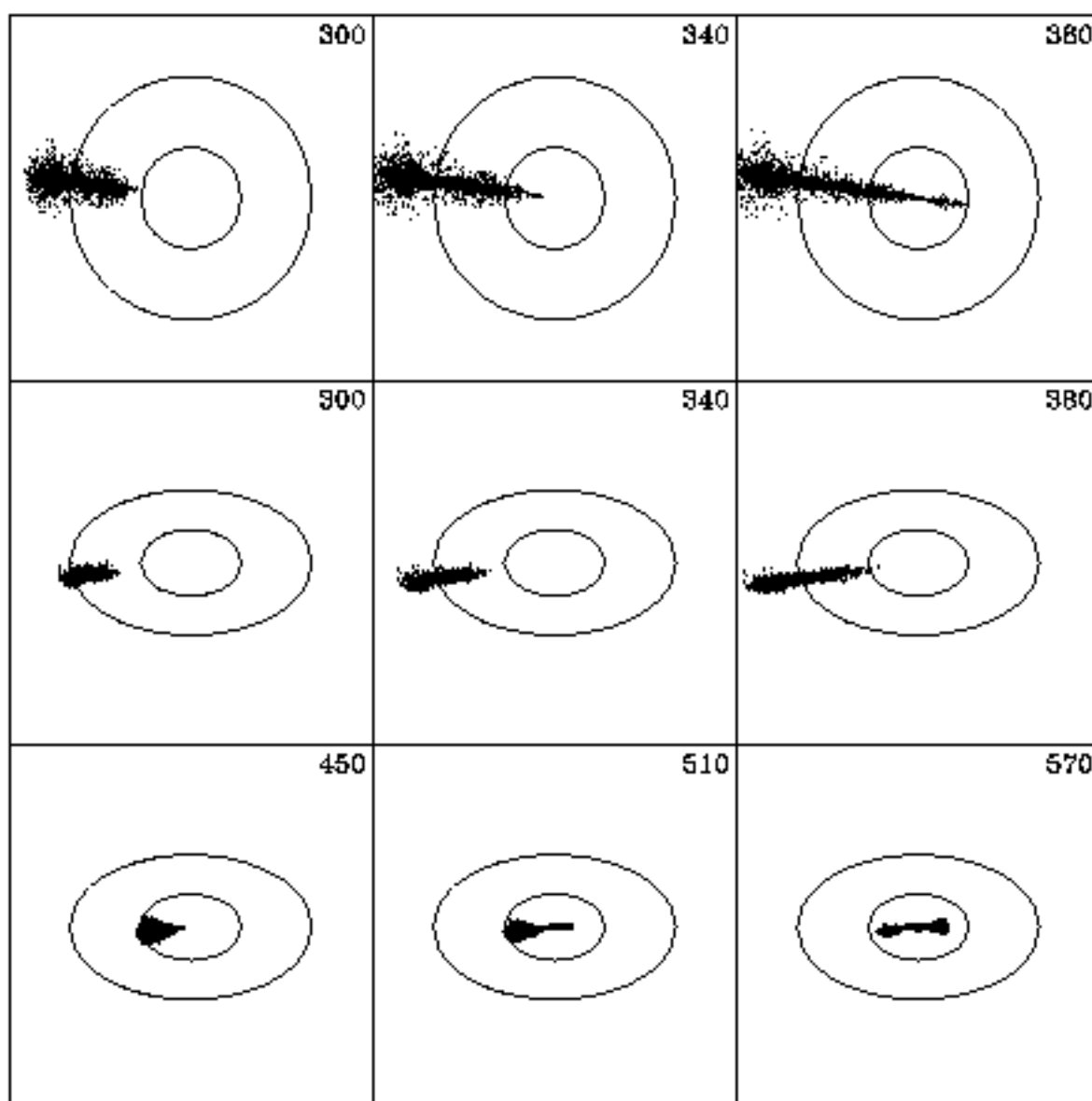
This figure "fig1.jpg" is available in "jpg" format from:

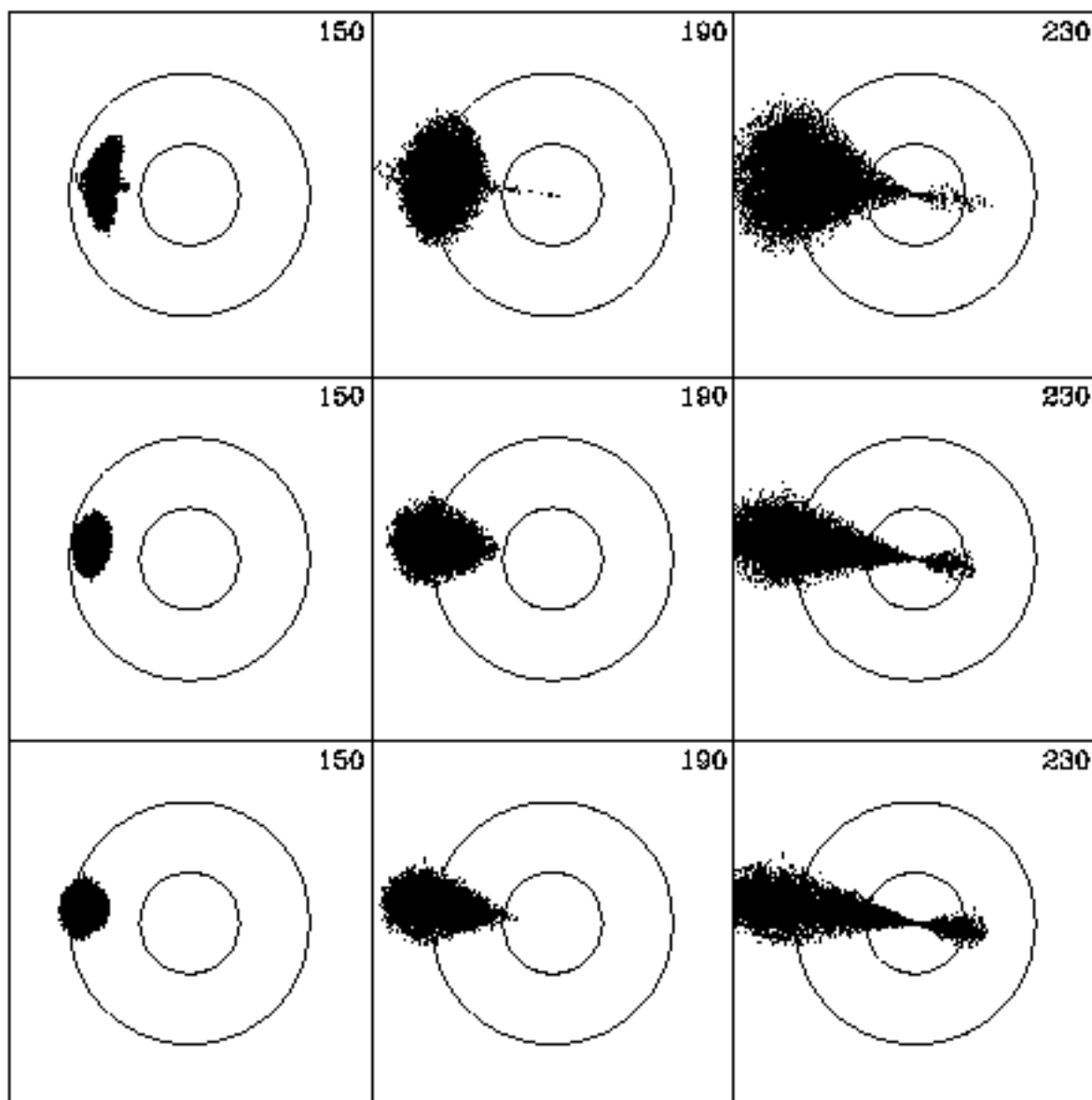
<http://arXiv.org/ps/astro-ph/9707084v1>

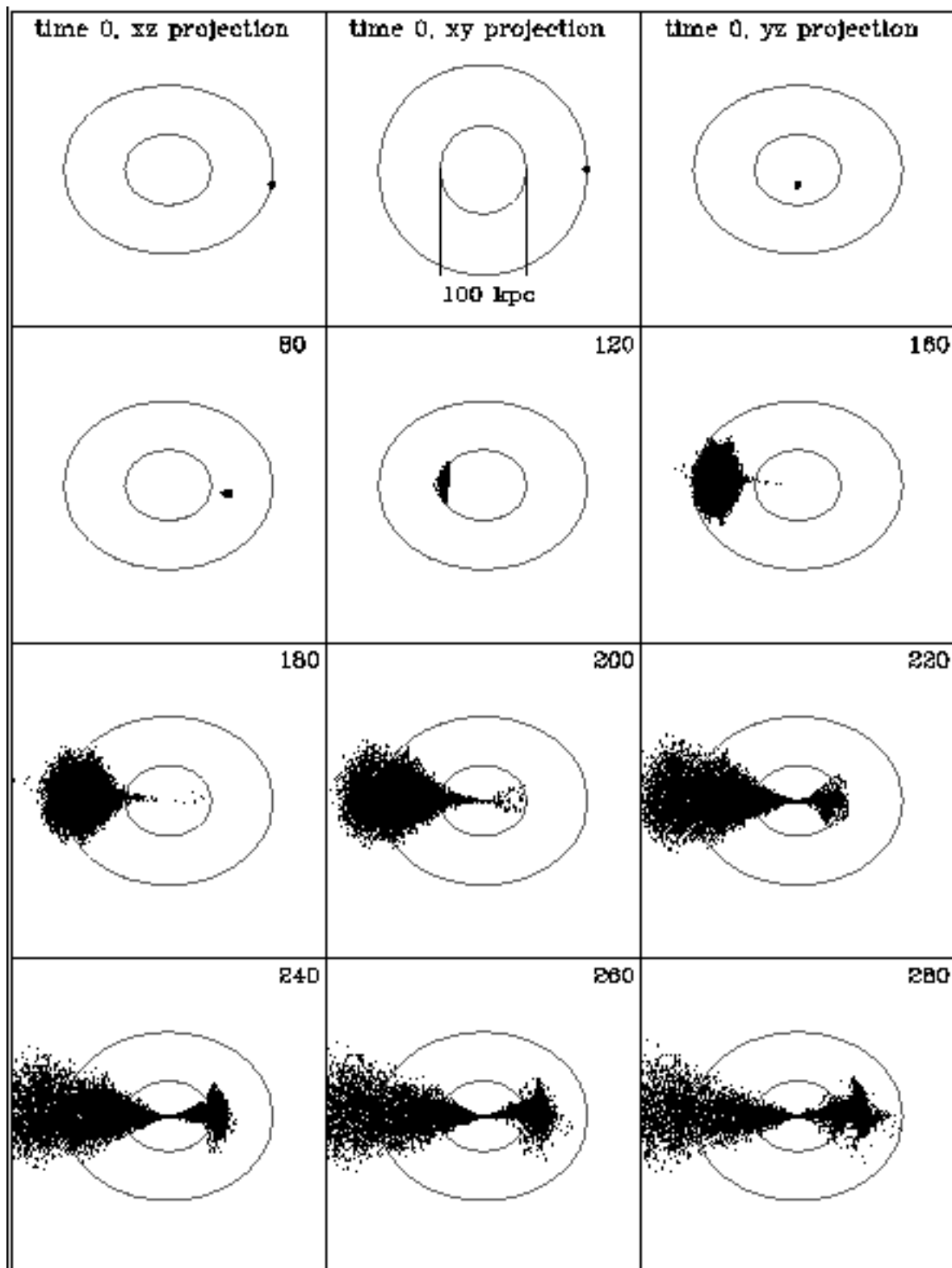
This figure "fig2.jpg" is available in "jpg" format from:

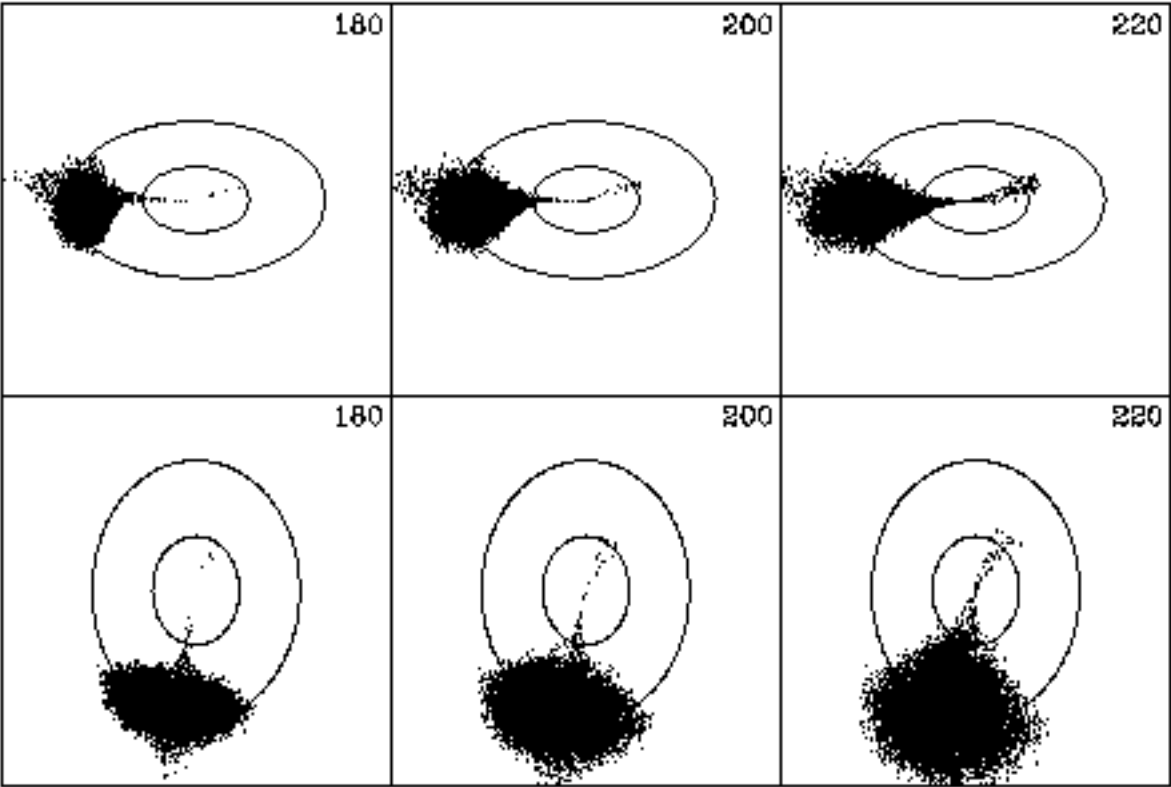
<http://arXiv.org/ps/astro-ph/9707084v1>

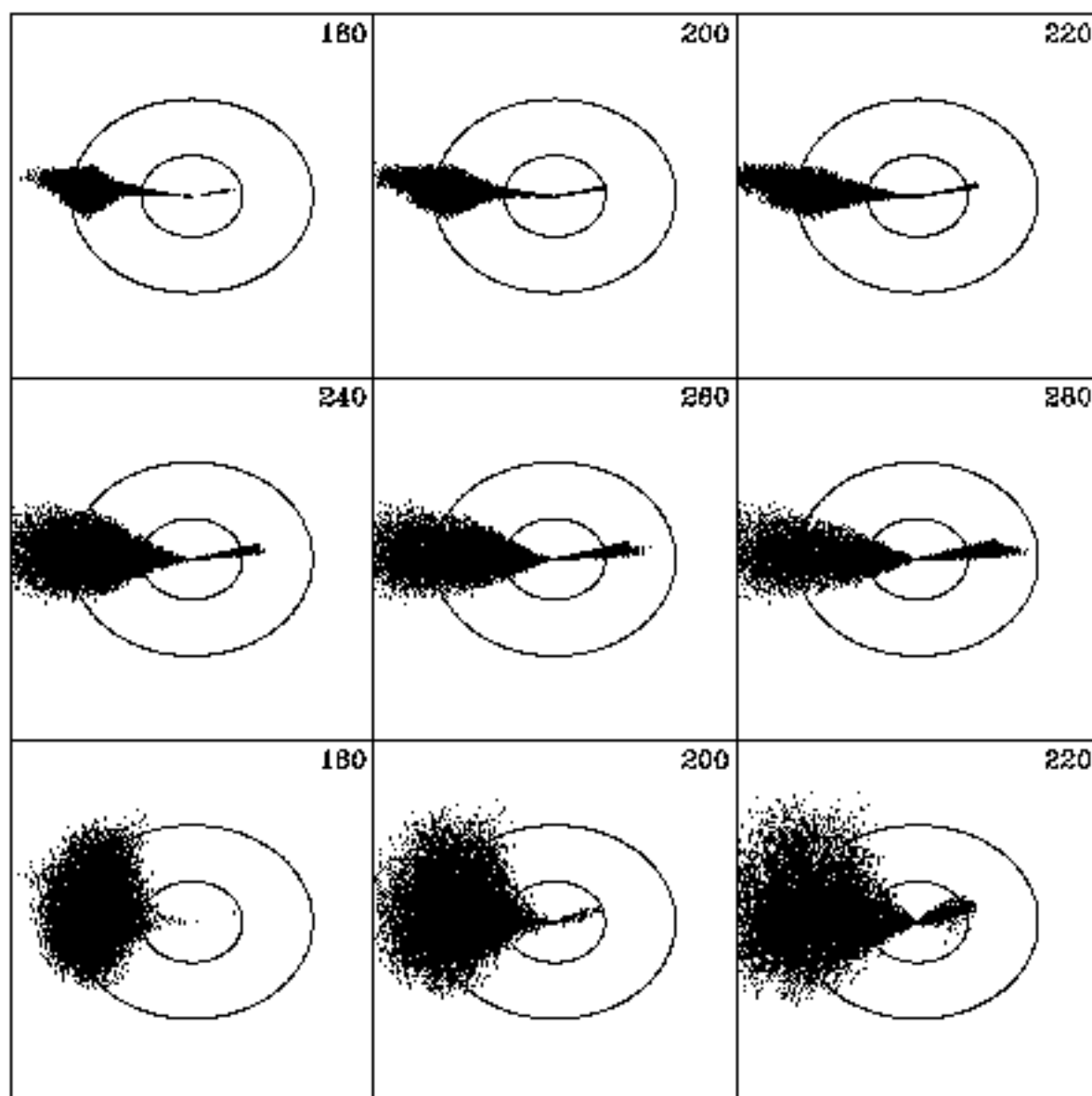


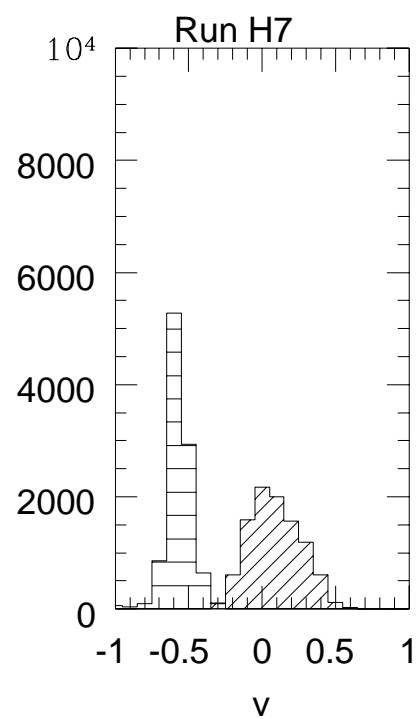
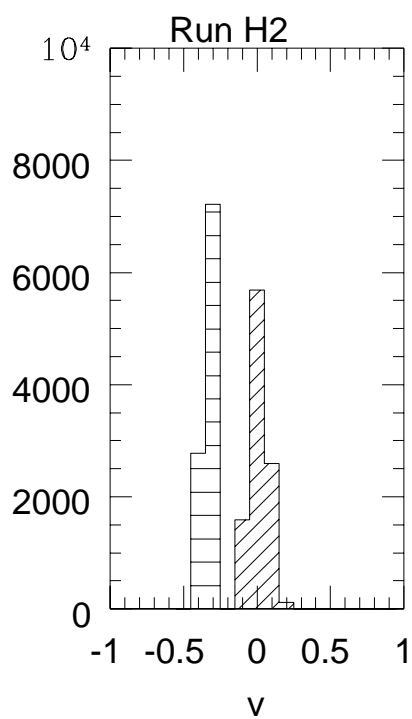
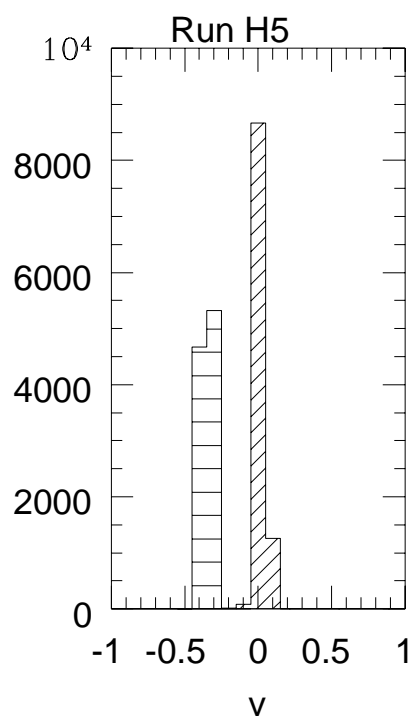
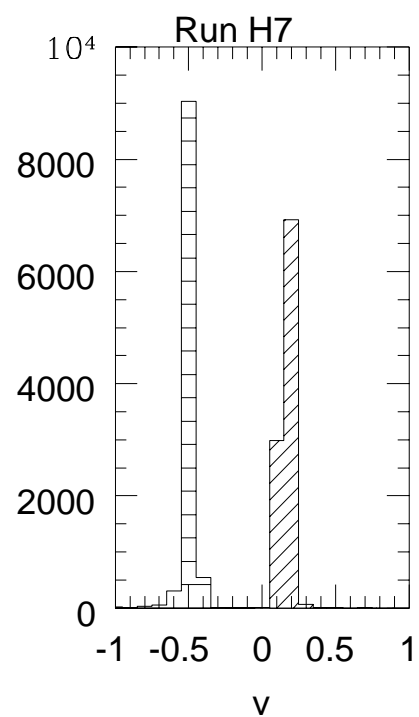
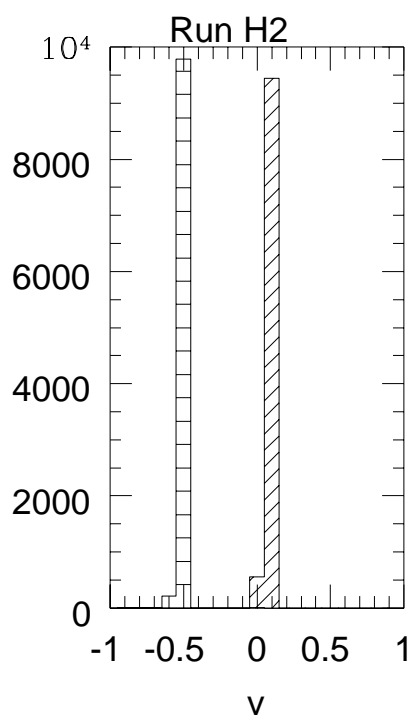
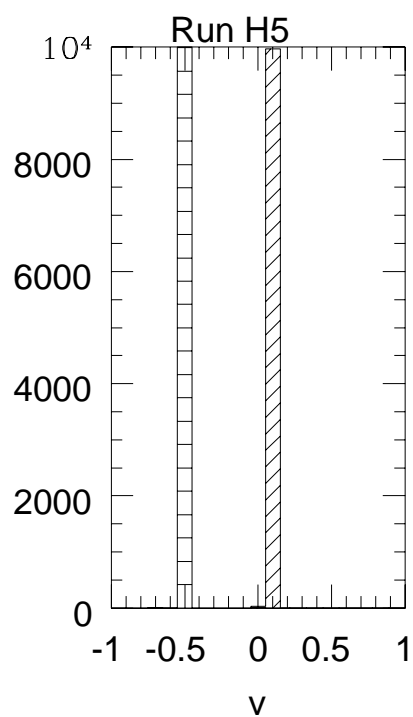


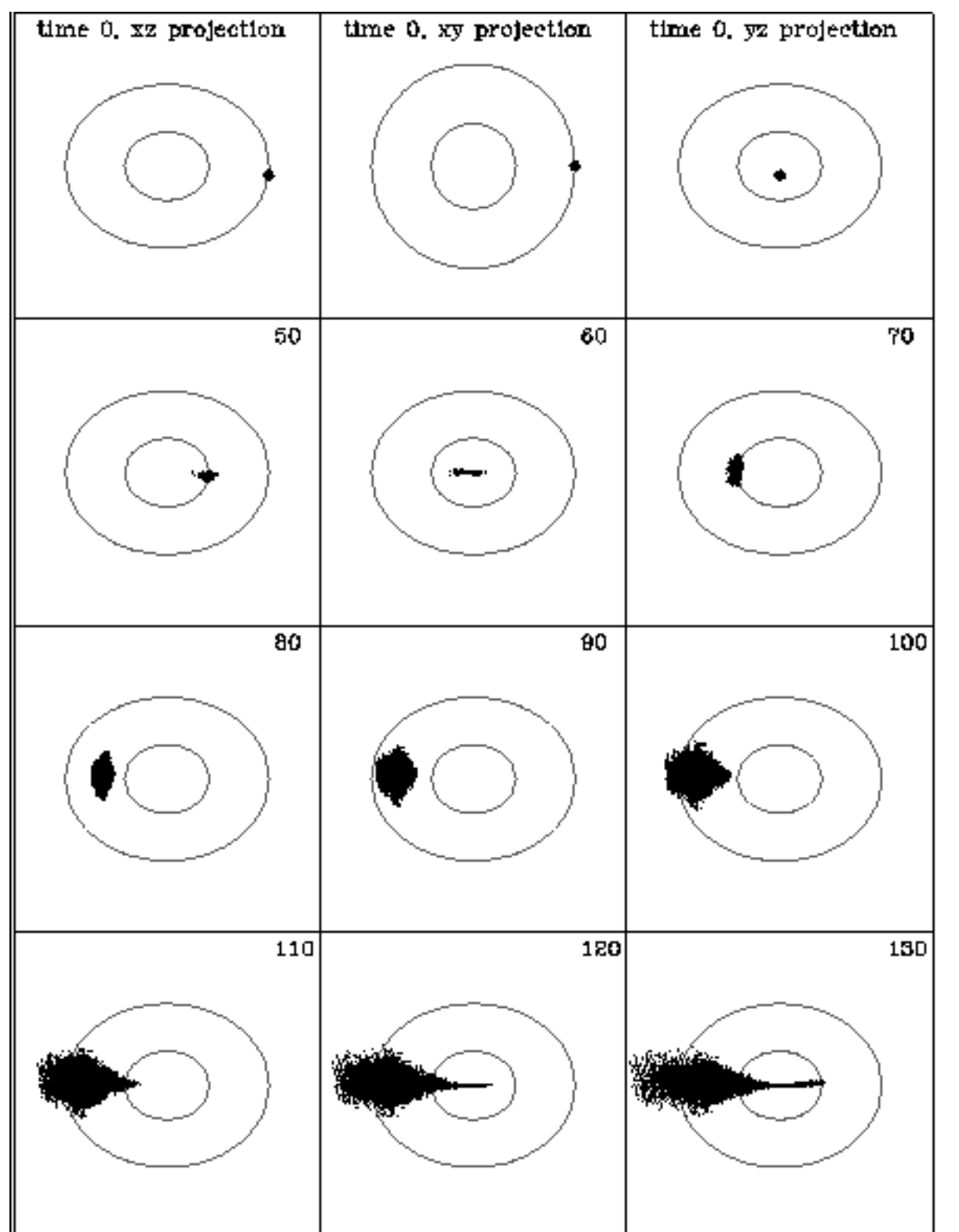


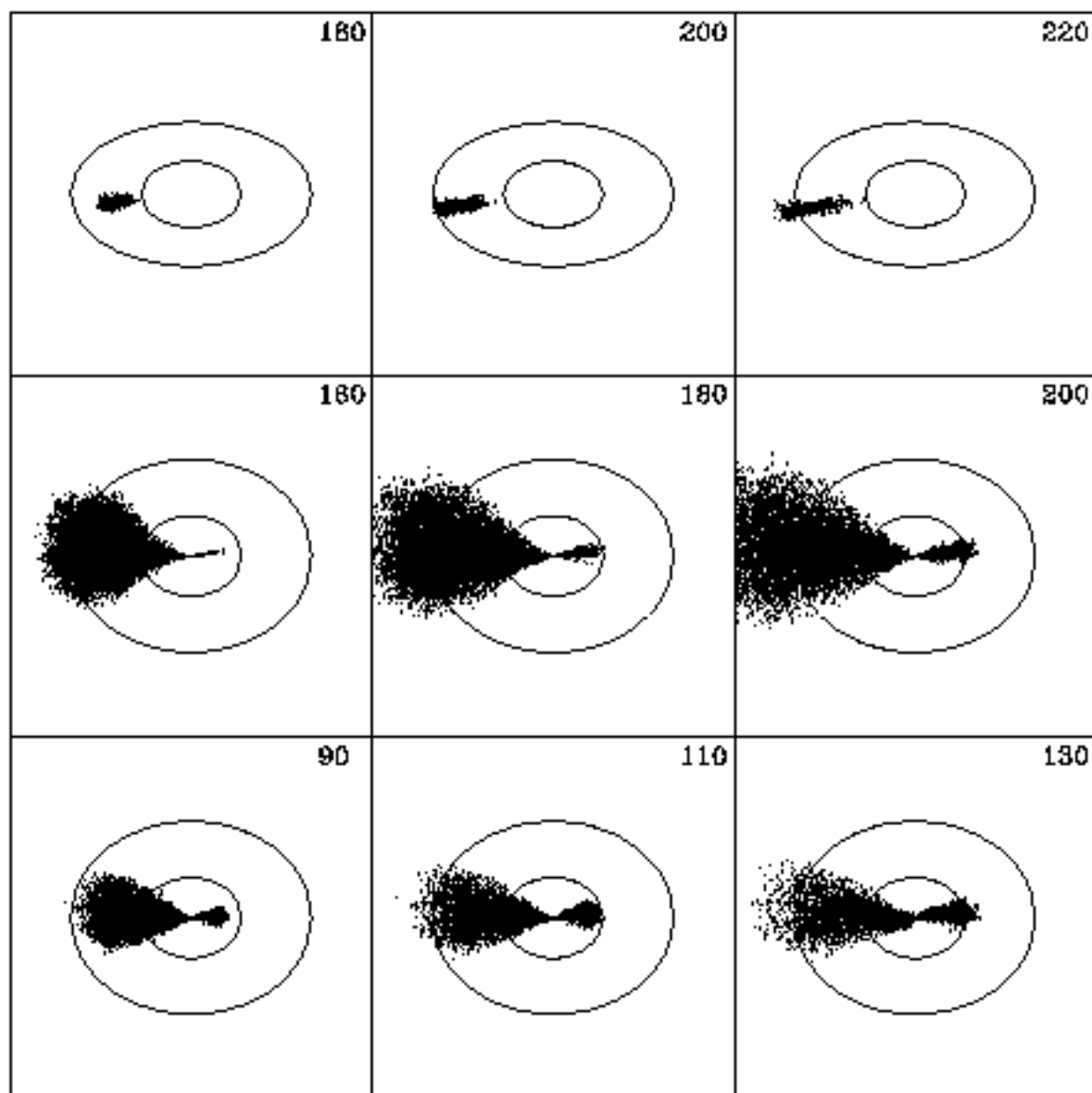


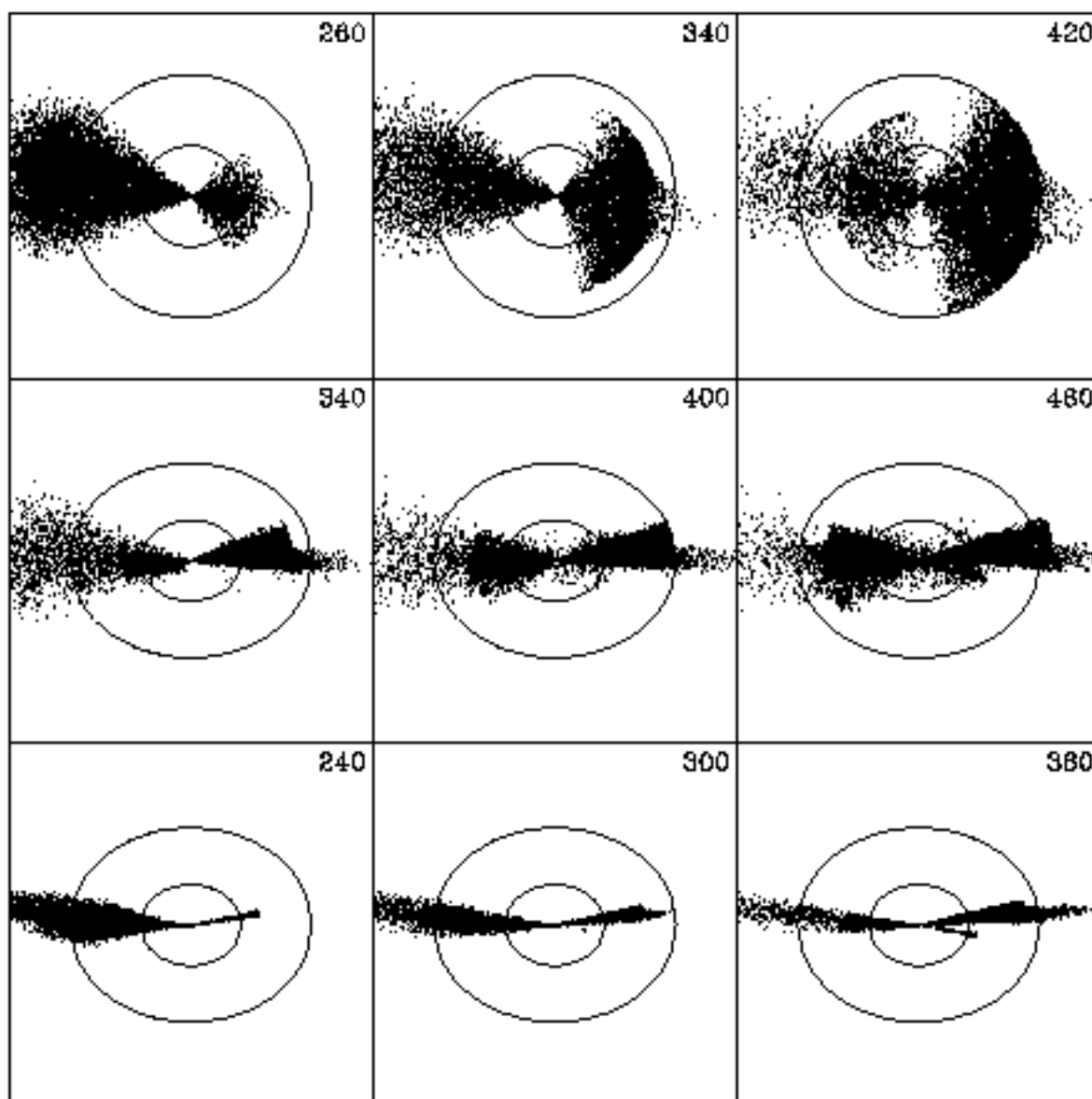


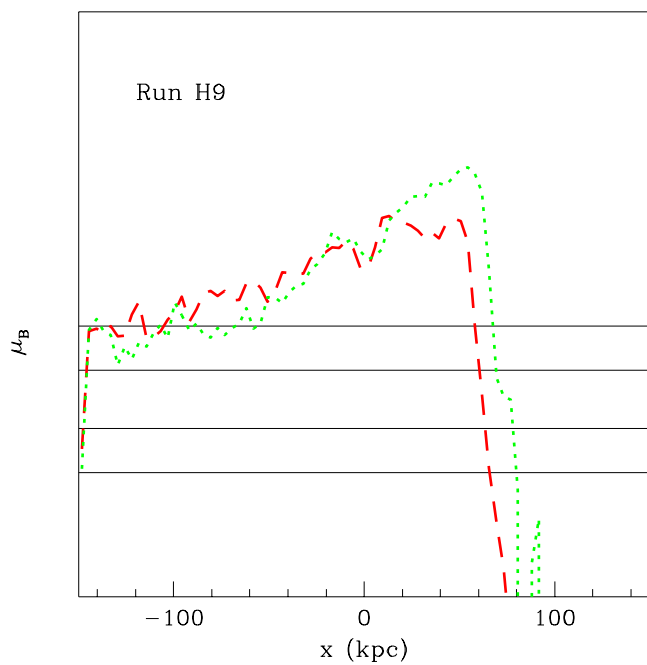
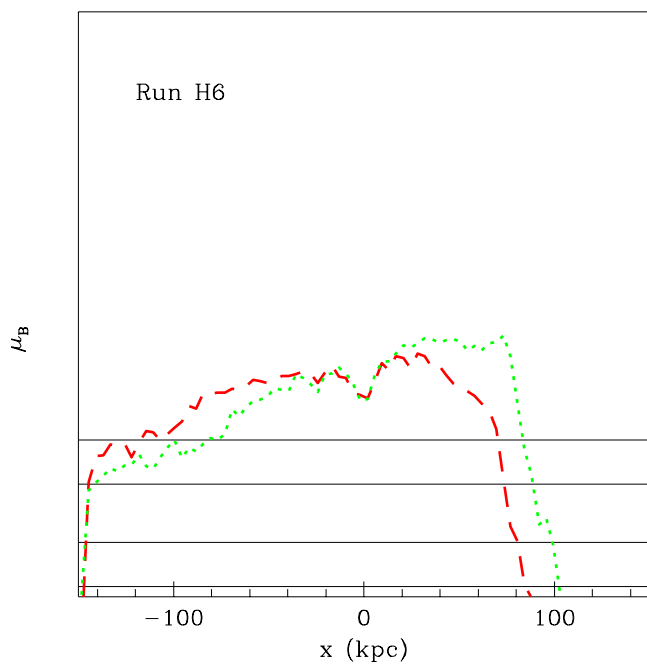
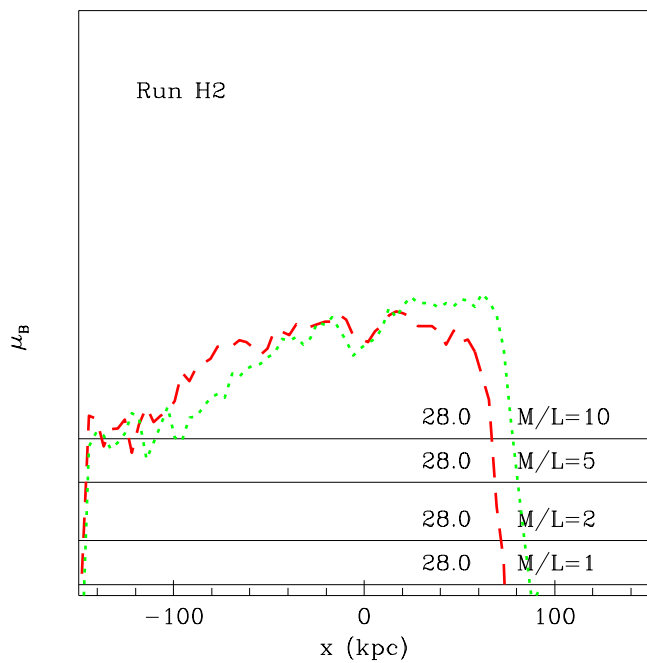
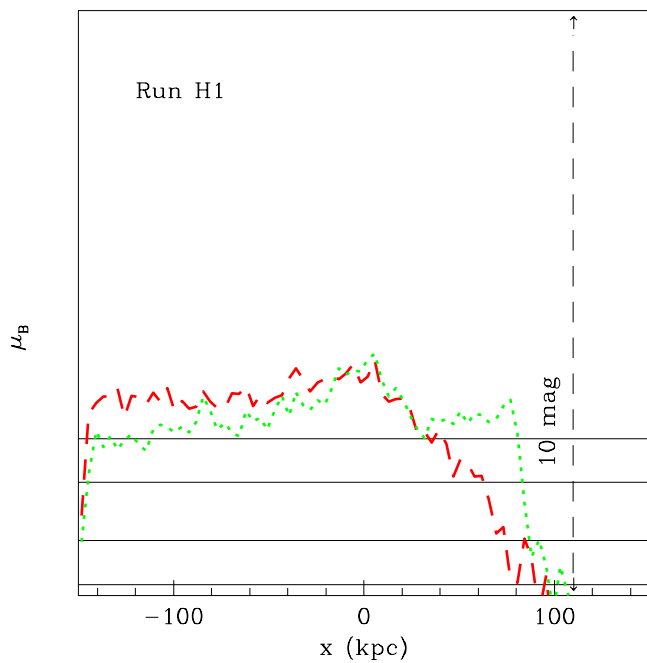


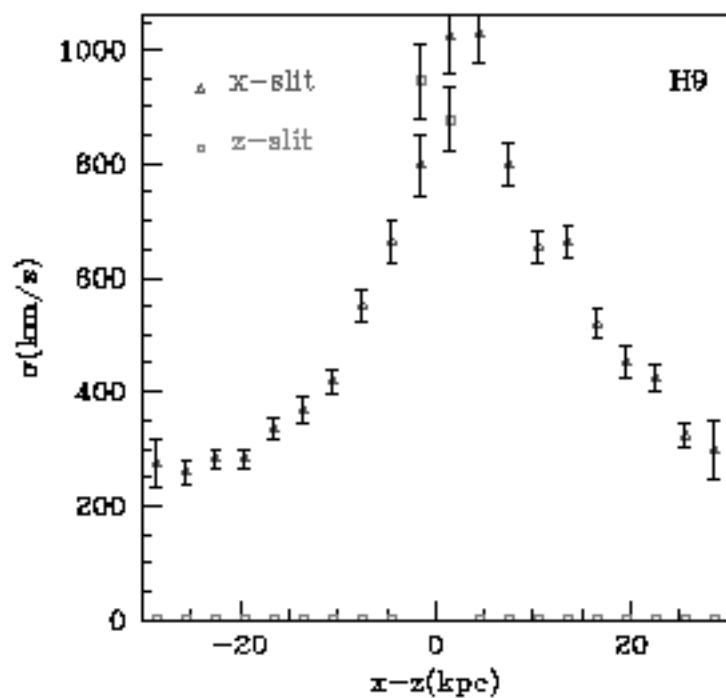
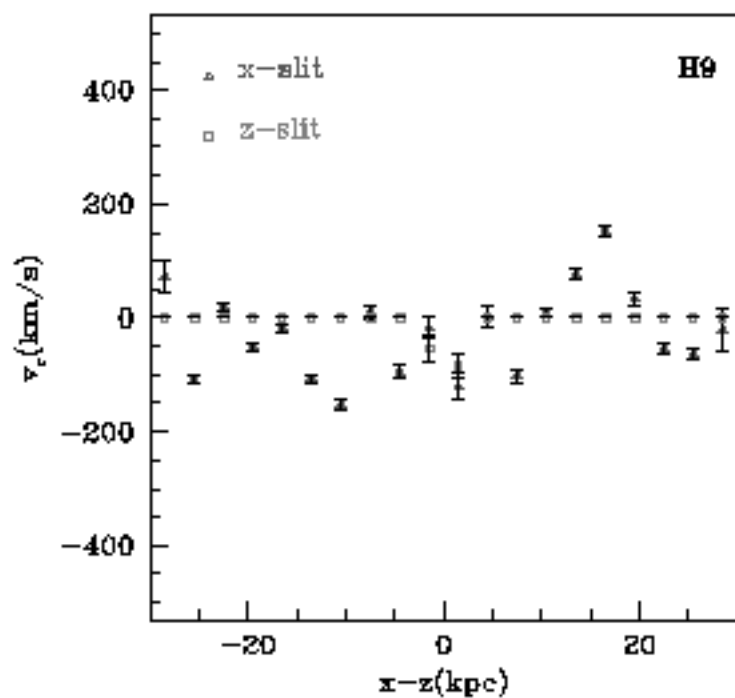
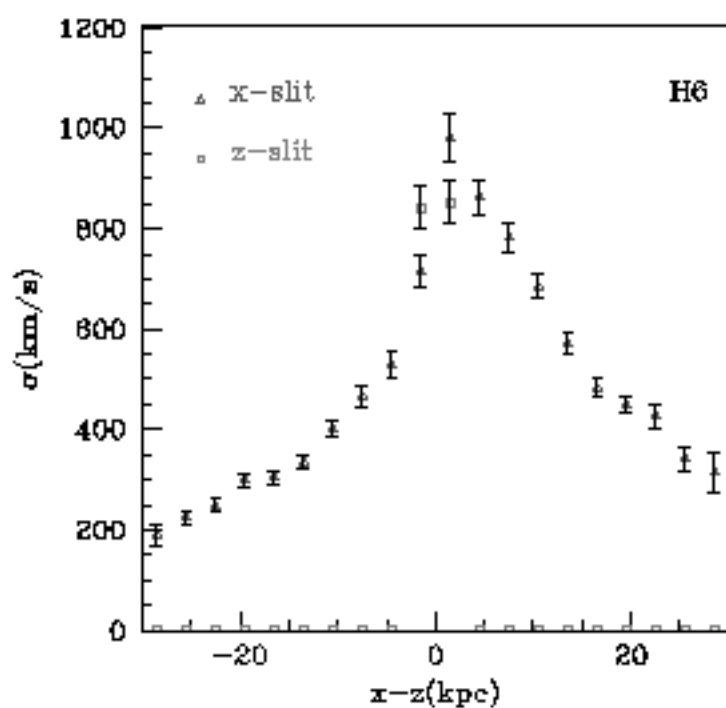
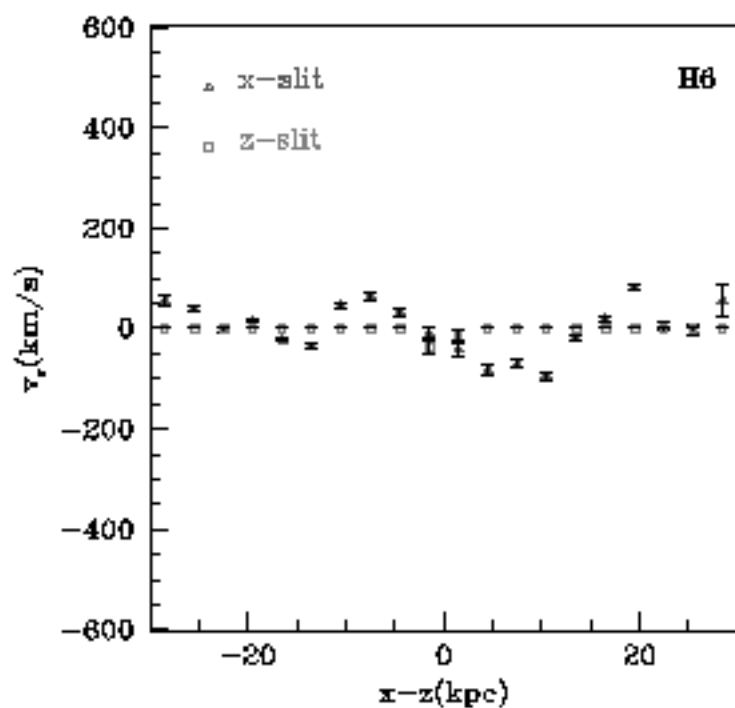












This figure "fig15.jpg" is available in "jpg" format from:

<http://arXiv.org/ps/astro-ph/9707084v1>